DESIGN PRINCIPLES FOR LARGE FOIL BEARINGS BASED ON SCALING LAWS: ANALYSES AND EXPERIMENT

by

SRIKANTH HONAVARA PRASAD

Presented to the Faculty of the Graduate School of
The University of Texas at Arlington in Partial Fulfillment
of the Requirements for the Degree of

DOCTOR OF PHILOSOPHY

THE UNIVERSITY OF TEXAS AT ARLINGTON
December 2018

Copyright © by Srikanth Honavara Prasad 2018

All Rights Reserved

ACKNOWLEDGEMENTS

I would like to thank Dr. Daejong Kim who has been my advisor for many years. His clarity of thought and attention to detail has influenced me significantly. Without his support, this journey would not have been possible. I would like to thank Dr. Alan Bowling, Dr. Andrey Beyle, Dr. Bo Wang, and Dr. Kyungsuk Yum for helping me enhance the quality of the manuscript.

Special thanks to Dr. Yongliang Wang for all the help in setting up the test rig. Many thanks to Dr. Nguyen Latrey for helping me in making the bearing. In addition, I would like to thank all the current and former members of TESLAB for their endless friendship and help at one stage or another. The financial support of Bellkim Energy LLC and the University of Texas at Arlington is also acknowledged.

Kermit Baird manufactured many of the parts very quickly and helped provide clarity into manufacturing process. His help and generosity deserve special appreciation. Finally, I would like to thank my family and friends for their love and understanding.

November 26, 2018

ABSTRACT

DESIGN PRINCIPLES FOR LARGE FOIL BEARINGS BASED ON SCALING LAWS: ANALYSES AND EXPERIMENT

Srikanth Honavara Prasad, PhD

The University of Texas at Arlington, 2018

Supervising Professor: Daejong Kim

Gas foil bearings are used for supporting high speed turbomachinery systems. They are characterized by complex physical and thermal interactions between the lubricating fluid and the structural elements. Mathematically, the behavior of such systems is governed by nonlinear partial differential equations and pose substantial computational challenges. However, their potential applications in aerospace systems and power generation systems have renewed research and development efforts aimed at simplifying their design and analyses methods. Commercialization of gas foil bearings in Mega Watt scale applications necessitate the development of simple tools for estimating bearing design parameters such as load capacity, radial clearance, and support structure stiffness, etc.

NASA engineers developed the “rule of thumb” guidelines for estimating foil bearing load capacity based on the bearing projected area, operating speed, and design considerations. The load capacity relation was based on experimental data available at that time (2000). Other researchers used the “rule of thumb” to develop scaling laws for estimating foil bearing design parameters such as radial clearance and support structure stiffness. However, the usefulness of scaling laws in the design of large foil bearings had not been demonstrated previously.

In this dissertation, a four degree of freedom (4-DOF) rotordynamic analysis performed for typical double overhang turbomachinery systems employing foil bearings designed following the scaling laws is presented. Further, case studies to show the feasibility of foil bearings for applications in Mega Watt range turbo blowers and turbo compressors is also presented. In addition, a full-scale experimental test rig for a 200 mm hybrid air foil bearing is designed and constructed for verifying the application of scaling laws in bearing design. The results of preliminary tests characterizing zero speed stiffness characteristics are presented.

TABLE OF CONTENTS

LIST OF ILLUSTRATIONS

LIST OF TABLES

Chapter 1

INTRODUCTION

Gas foil bearings (GFB) are used for supporting high speed turbomachinery systems. The main advantage of GFB over conventional oil lubricated bearings is the elimination of the oil sub-systems. The oil sub-systems constitute 8-13% of the total weight of a typical turbofan engine [1]. Therefore, their elimination helps reduce the total weight and corresponding fuel consumption in aerospace applications. Further, GFB offer higher operating speeds, improved reliability, and a wide choice of process gases that can be used for lubrication.

The heating, cooling, and pressurization of aircrafts is carried out using high speed rotating machines known as air cycle machines (ACM). Most modern aircrafts employ GFB for supporting the rotating components in the ACM [2]. Improvements in manufacturing processes and advances in the design of GFB have made them suitable candidates for potential use in other aerospace and power generation applications. These systems range from small sized turbomachines (kilo Watt range) to large sized systems (Mega Watt range) operating at high speeds. Scale-up or scale-down of a proven GFB could help in rapid prototyping for a wide range of applications. However, scale-up or scale-down of a proven GFB is quite challenging because of the inherent complex coupling of fluid, thermal, and structural phenomena. The resulting system is mathematically described by nonlinear partial differential equations. Therefore, the design of new bearings requires extensive computational effort in determining bearing parameters. The feasibility of new bearings can also be experimentally determined. However, rigorous experimental testing is costly and may not be practical for many bearing designers.

These challenges present opportunities for investigating methods for simplifying bearing design and developing tools for their performance estimation. A widely used approach for solving problems of this nature is to look for trends in existing bearings that have been successfully used for various applications. However, an understanding of the nonlinearities involved is essential for interpreting trends and developing guidelines. Therefore, the key features of GFB are discussed in the next section to highlight the underlying physics.

1.1 Radial Gas Foil Bearings

The presence of a compliant support structure distinguishes a GFB from a rigid journal bearing. A typical GFB consists of a compliant support structure resting within a rigid sleeve as shown in Figure 1. The clearance between the journal and the sleeve has been greatly exaggerated to indicate the relative position of the journal with respect to complaint structure and the rigid sleeve.

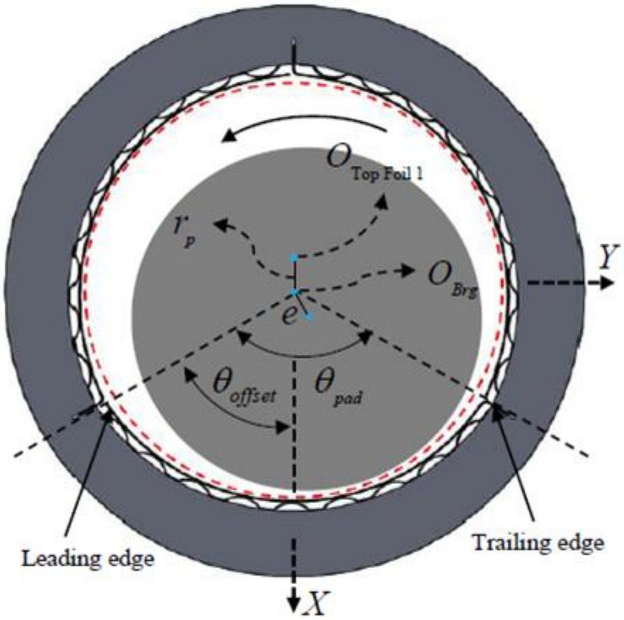

Figure 1 Radial 3-pad GFB [3]

The schematic diagram in Figure 1 shows a three-pad GFB with compliant structure comprising three sets of top foils supported by corresponding bump foils. Three-pad configuration offers better stability characteristics over conventional single pad configuration (with only one top foil and corresponding bump foil). The distance between the journal center and the pad centers is called the “pad preload offset”. In practice, preload is achieved by machining the inner surface of the sleeve (for each pad) offset from the outside diameter. As the journal rotates within the bearing, its center does not coincide with the bearing center. The distance between the journal center and the bearing center is called the “eccentricity”. It is often non-dimensionalized with the bearing clearance. The ratio of eccentricity to the bearing clearance is called the “eccentricity ratio”. Eccentricity ratio always has values between zero and one with zero indicating coincident bearing and journal centers while one indicates journal in physical contact with the bearing surface.

When the journal is stationary, the elastic nature of top foils and manufacturing errors result in weak contact between the journal and top foils. As the journal starts rotating, it imparts kinetic energy to the surrounding gas. Beyond a certain speed, the circumferential velocity of the fluid separates the journal from the top foils creating a converging-diverging section as shown Figure 1. This condition is called “lift-off”. The flow of gas in the converging-diverging section between the journal and the top foil is characterized by the conversion of kinetic energy of the fluid into local rise in pressure which manifests as the load capacity. The load capacity of a bearing is defined as the maximum load that can be supported by the bearing under steady operation. It is important to note that in the absence of any external injection of pressurized gas, the load capacity of the bearing exists only because of the flow through the converging diverging section and the resulting asymmetric pressure profile. The profile of the converging diverging section depends on the design clearance, the journal position within the bearing, the deflection of the supporting foils and preload effects. Therefore, it follows that the bearing wouldn’t have any load capacity if the journal and bearing were concentric as the pressure would be identical around the circumference. This type of bearing is often called self-acting bearing and the mode of operation is called “hydrodynamic lubrication”. The load capacity of GFB is much smaller than their oil lubricated counterparts because gases have lower viscosities and are compressible [4]. Externally pressurized air is often injected radially to prevent excessive wear during start-up or coast-down for bearings subjected to significant vertical loading (i.e., large rotors). This mode of operation is called “hydrostatic lubrication”. When gas foil bearings are operated with the combined effects of hydrodynamic and hydrostatic pressurization, the resulting bearing is called “Hybrid gas foil bearing” or “Hybrid air foil bearing” (HAFB) when gas used is air.

The angle between the resultant radial reaction force vector and eccentricity, measured in the direction of rotation, is called the “attitude angle”. This is also the angle between the line joining the bearing and the journal centers and the loading direction. The reaction force can be resolved into radial and tangential components. The components of the reaction force are modeled as forces due spring elements that undergo small deflections. The component of reaction force in the radial direction acts as a restoring force and its rate of change with corresponding displacement is termed as “direct stiffness”. The tangential component of the reaction force drives the journal into an orbit around the bearing center (precession) and its rate of change with corresponding displacement is called “cross coupled stiffness”. The direct and tangential stiffness terms can be resolved along the coordinate axes (i.e., X and Y directions).

Instability in the bearing results from the effects of tangential forces acting on the journal. The rotation of the journal produces a circulation of the gas in the clearance between the journal and the bearing. The average velocity of this circulation is almost 0.5 times the velocity of the journal for an infinitely long bearing. However, in finite bearings, gas is lost due to end leakage and the average circulation is less than 0.5 times the journal speed. This fluid motion also contributes to the overall motion of the journal and under certain conditions, leads to self-excited vibration of the journal (large lateral vibration). The frequency of the journal orbit is normally less than half the frequency of the journal rotation and it is called “Fractional Frequency Whirl”. For a given bearing geometry, the journal orbit may be stable, neutrally stable, or unstable depending on the speed and load condition.

The bearing geometry consideration involves design and selection of support structure to enhance the stiffness, damping and thermal characteristics of the bearing. Further, the design clearance must be chosen such that the bearing can accommodate the effects of centrifugal growth of the shaft at high speeds and any thermal expansion that may occur due to viscous dissipation. These criteria affect both the static and dynamic performance of bearings.

1.2 Literature Review

Based on the discussion on journal bearings, it is clear that the design and analysis of radial gas foil bearings is challenging because of the complex physical phenomena. Numerical analyses are computationally intensive and experimental testing is costly. Existing machines cannot be directly retrofitted with existing gas foil bearings. The turbomachinery system needs to be considered in its entirety for successful implementation of gas foil bearings. These challenges have prompted researchers to develop simple tools to address initial design guidelines for gas foil bearings.

DellaCorte and Valco [5] presented a simple “rule of thumb” (ROT) for load capacity estimation based on experimentally available data for gas foil bearings. They found that the load capacity was dependent on the surface speed of the shaft, the projected area of the bearing and the design of the bearing. DellaCorte [6] extended the ROT guideline to include the bearing stiffness and damping coefficients. These guidelines were based on experimental data from existing literature at the time of the development and therefore represent approximate relationships only for certain range of bearing sizes. These guidelines may not be accurate for large sized bearings or those operating under extreme conditions [3]. One of the reasons the guidelines may not hold is because of the "cube-square law" [7]- the load capacity is proportional to the square of the characteristic dimension while the rotor weight is proportional to the third power of the characteristic dimension. Further, the load capacity has an approximately linear relationship with speed only within a certain range of DN number (product of diameter in mm and speed in revolutions per minute (RPM)) [8]. Peng and Khonsari showed the linear relationship for a 38 mm bearing operating at a DN number of 3 million. The variation of load capacity in [N] with speed in [krpm] is also shown in Figure 2 for 100 mm bearing operating at DN number of 4 million. The DN number indicates the surface speed of the shaft. Therefore, at a particular DN number, bearings of different sizes will have the same surface speed. The higher the DN number, the greater is the shear experienced in the fluid film and higher is the viscous dissipation. Peng and Khonsari [9] also showed that the limiting load capacity for foil bearings occurs at DN number (>50 million) which is significantly beyond the range of conventional operating range (~3.5 million).

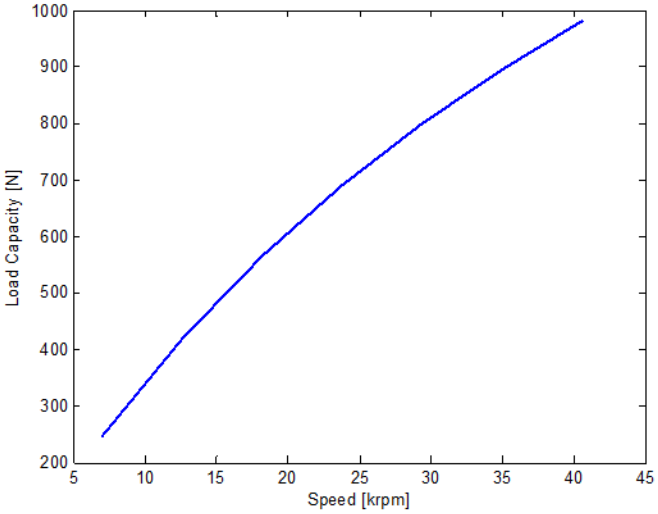

Figure 2 Variation of load capacity [N] with speed [krpm] for 100 mm bearing

Therefore, any ROT that is suggested for foil bearings must be interpreted with caution and all the dependencies must be carefully examined. Despite the limited applicability of ROT guidelines, they serve as invaluable starting point for new bearing designers. Tremendous savings in time and resources is obtained when a bearing designer has a reference bearing that can simply be scaled up or scaled down and modified as required. Some of the factors that must be taken into consideration while designing new bearings include radial clearance, support structure stiffness, damping and rotordynamics.

Radil et al. [10] performed load capacity tests on foil bearings and determined the effect of radial clearance on load capacity coefficient. Their tests showed the sensitivity of the load capacity coefficient to the radial clearance and that the maximum load capacity coefficient occurs at a certain optimum radial clearance. Operation below the optimal radial clearance increases the possibility of thermal runaway while operation above the optimal clearance reduces the load capacity of the bearing. Their study did not consider the effects of radial clearance on dynamic characteristics including stiffness and damping of the bearing.

The scaling laws for dynamic behavior of ultra-short hydrostatic gas bearings were developed by Spakovszky and Liu for addressing micro-bearing design for MIT micro-devices [11]. This was achieved by finding hydrostatic stiffness, hydrodynamic stiffness, and damping, and then, deriving expressions for natural frequency and damping ratio. They also investigated the onset of whirl instability and provided a simple geometry dependence criterion for whirl ratio. Further, they developed design charts for linking fabrication tolerances, bearing performance, and rotor unbalance for minimum required whirl ratio.

The papers listed provide useful guidelines for estimating load capacity and bearing coefficients for certain gas bearings. However, there are no simple guidelines for choosing radial clearance and stiffness of structural support elements when scale-up or scale-down design of existing foil bearing is required. This issue was addressed by the authors in Ref. [3] and is also detailed in Chapter 2. The scaling relations in Ref. [3] are for initial design parameters of the bearing so that the foil bearings have adequate load capacity as the bearings are scaled up and scaled down from a well-designed bearing. However, the scaling laws do not provide enough information regarding rotordynamic stability of the foil bearings for double overhung rotor systems.

The importance of rotordynamic analysis for determining the stability of foil bearings is well known. In 1962, Rentzepis and Sternlicht [12] analytically investigated the regions of stability for bearings supporting rigid rotor systems under isothermal operation and determined the existence of a clearance ratio at which the stability characteristics are the lowest. Ausman used the product of pressure and film thickness as the dependent variable in the governing equation (linearized PH theory) to investigate half speed whirl [13, 14]. Cheng and Trumpler [15] employed Galerkin's method for determining the equilibrium position of journal center for a dynamical system supported by self-acting gas bearings. They presented the stability characteristics of plain cylindrical gas bearings of infinite length. The Galerkin's method simplifies the highly nonlinear partial differential equations governing the fluid film (Reynolds Equation) into a system of first order ordinary differential equations. This method was also used by Cheng and Pan [16] who investigated the stability characteristics of plain cylindrical gas bearings of finite length. However, their results were not adequate for high eccentricity ratios and large L/D values. Elrod and Castelli [17] numerically solved the complete set of nonlinear equations for fluid and the shaft motions and their evolution in time in order to evaluate the orbit of the journal. This numerical method (also known as Orbit Method) mimics a test rig and allows a wide variety of numerical "experiments" to be performed. In 1999, Piekos [7] employed a pseudo spectral formulation of the Reynolds equation for improving the efficiency of the orbit simulation. The resulting solver was used for designing bearings for micro-fabricated turbomachines that were being developed at MIT.

In recent years, the application of foil bearings to large systems has gained increased attention. Heshmat and Xu [18] showed the performance of a 150 mm hybrid foil/magnetic bearing and demonstrated operation under hybrid mode at DN number of 4 million. Salehi et al. [19] experimentally determined the dynamic structural stiffness and damping characteristics of a 216 mm bearing by exciting a non-rotating journal with a shaker. Ertas et al. [20] designed a test rig for evaluating gas bearings in the range 70 mm- 120 mm diameter operating between 40,000 and 80,000 rpm for aircraft engine applications. Delgado [21] used a motion control test rig and experimentally evaluated the dynamic performance of a 110 mm hybrid gas bearing.

1.3 Layout of the Dissertation

Some important observations can be made based on the papers listed in the literature review. While designing gas foil bearings, rotordynamic considerations are important to determine the stability of the bearings over a wide range of operating speeds. In addition, literature on the design performance evaluation, and testing of large foil bearings is lacking.

Therefore, the following layout is employed in this dissertation. Chapter 2 revisits the scaling laws that were previously developed (Ref. [3]) and provides a starting point for further analysis. The scaling laws for support structure stiffness and radial clearance for radial foil bearings are presented. Chapter 3 serves as an extension of Ref.[3] and presents the rotor-dynamic performance of large turbomachinery systems with foil bearings designed using the scaling laws for radial clearance and support structure stiffness. Chapter 4 presents the details of an experimental test rig that was designed, manufactured and assembled to test a 200 mm hybrid air foil bearing developed following the scaling laws.

Chapter 2

SCALING LAWS FOR RADIAL FOIL BEARINGS

The focus of this chapter is the development of scaling laws for radial clearance and support structure stiffness of radial foil bearings. Many details presented in this chapter may also be found in Ref. [3].

2.1 Scaling Laws for Radial Clearance

The load carrying capacity of a foil bearing is defined as the maximum load that can be supported at a constant speed of operation. As the speed is increased, the effect of viscous pumping action results in increased load capacity. The pressure gradient between the film and the ambient produces edge leakage in the bearing. Due to this leakage, the local pressure at the edge is much lower than the peak pressure in the bearing. Edge leakage also reduces the local film thickness. When the film thickness approaches the average roughness of the solid surfaces (foil and shaft), there may be local contact resulting in wear and damage. Based on these considerations, DellaCorte and Valco [5] proposed the load capacity relationship for foil bearing as a function of the average surface speed of the shaft, the projected area and the design features of the bearing.

$$F = \xi_o L D^2 N \tag{1}$$

The load capacity of a bearing operating at a certain speed is also given by the integration of the average pressure in the film over the bearing projected area.

$$F = \int p dA = p_{avg} L D \tag{2}$$

The non-dimensional form of the compressible Reynolds Equation is given by:

$$\frac{\partial}{\partial \theta}\left(PH^3 \frac{\partial P}{\partial \theta}\right) + \frac{\partial}{\partial Z}\left(PH^3 \frac{\partial P}{\partial Z}\right) = \Lambda\left[\frac{\partial}{\partial \theta}(PH) + 2\frac{\partial}{\partial \tau}(PH)\right] \tag{3}$$

The pressure terms on the left-hand side of the equation are of order 2 while the pressure terms on the right hand side of the equation are of order 1. Within a certain range of speeds, the average pressure is proportional to the bearing number. Therefore,

$$p_{avg} \propto \Lambda = \left(\frac{6\mu}{p_a}\frac{2\pi N}{60}\right)\left(\frac{R}{C}\right)^2 = N\left(\frac{\pi\mu}{5p_a}\right)\left(\frac{R}{C}\right)^2 \tag{4}$$

Consequently, the load capacity of a foil bearing may be rewritten as:

$$F = LDp_{avg} = k_{f0}LD^2N\left(\frac{\pi\mu}{10p_a}\right)\left(\frac{R}{C^2}\right) \tag{5}$$

Grouping of constant terms results in simpler form of the equation:

$$F = k_f LD^2N\left(\frac{R}{C^2}\right) \tag{6}$$

The load capacity from DellaCorte and Valco [5] must match the load capacity determined from the average bearing pressure. Therefore,

$$\xi_o = k_f\left(\frac{R}{C^2}\right) \tag{7}$$

Therefore, the clearance is proportional to the square root of the bearing size.

$$\frac{R}{C^2} = \text{constant} \tag{8}$$

The result can be used for selection of initial nominal clearance of foil bearings with different sizes if a good reference design is available or known in prior. For example, if C_1 and R_1 are clearance and radius of certain well-designed foil bearing, clearance of a foil bearing with R_2 (but the same type as the referenced first bearing) can be chosen as

$$C_2 = C_1\sqrt{\frac{R_2}{R_1}} \tag{9}$$

2.2 Scaling Laws for Support Structure Stiffness

Structural support structure of the foil bearings takes various forms such as corrugated bump foils, multi-leafs, elastomeric material, metal meshes, etc. Because of highly non-linear and complicated nature of those support structures, they are often modeled as a series of inertia-less mechanical elements consisting of linear spring and viscous damper for simplicity of analysis:

$$f_b = pA_0 = k_b\delta + c_b\frac{d\delta}{dt} \tag{10}$$

where, $A_0 = 2\pi RL/N_{grid}$ is the bearing surface area covered by one support element (N_{grid} is the total number of the inertia-less linear spring/damper in computational domain), c_b is equivalent viscous damping and δ is the deflection of the structure. Using non dimensional terms, $S = \delta/C$, Eq. (10) becomes:

$$P = K_b\left[S + \eta\frac{dS}{d\tau}\right] \tag{11}$$

where, K_b represents the non-dimensional stiffness, and it is found to be:

$$K_b = \frac{k_bC}{p_aA_0} = \frac{N_{grid}}{2\pi p_a}\left(\frac{C^2}{R}\right)\frac{k_b}{CL} = \frac{N_{grid}}{4\pi p_a}\left(\frac{C^2}{R}\right)\frac{k_b}{CR} \tag{12}$$

In Eq. (12), $L = D = 2R$ has been assumed. It can be further assumed that the same numerical value of N_{grid} can be used for computational modeling of the foil bearing's performance regardless of the physical size of the bearing as long as the bearing type is identical. Because K_b is scale-invariant stiffness (constant) of the support structure and C^2/R is also constant from Eq. (8), it is concluded that :

$$\frac{k_b}{CR} = \text{constant} \tag{13}$$

Eq. (8) can be used for eliminating the operating clearance from Eq. (13):

$$\frac{k_b}{CR} = \text{constant} \quad \Rightarrow \frac{k_b}{CR}\left(\frac{C}{\sqrt{R}}\right) = \text{constant} \quad \Rightarrow k_b \propto R^{1.5} \tag{14}$$

From Eq. (14), the support stiffness is related to bearing size as:

$$\frac{k_{b,1}}{R_1^{1.5}} = \frac{k_{b,2}}{R_2^{1.5}} \qquad \Rightarrow \qquad k_{b,2} = k_{b,1}\left(\frac{R_2}{R_1}\right)^{\frac{3}{2}} \tag{15}$$

The above scaling law for the support structure's stiffness is based on the assumption that N_{grid} is constant. Therefore, k_b represents stiffness of entire physical structure underneath A_0. Another scaling law in terms of areal stiffness, i.e., stiffness per unit area (k_b / A_o) can also be found. Using the definition of areal stiffness, Eq. (14) and Eq. (8):

$$k_{b\_areal} = \frac{k_b}{2\pi RL / N_{grid}} = \left(\frac{N_{grid}}{2\pi}\right)\left(\frac{C^2}{R}\right)\left(\frac{k_b}{CR}\right)\frac{R}{LC} \tag{16}$$

Because the first, second and third terms in the far right expression of above equation are all constant, and $C \propto \sqrt{R}$ from Eq. (8) and $L \approx 2R$, it is found that

$$k_{b\_areal} \propto \frac{R}{LC} \propto \frac{1}{\sqrt{R}} \tag{17}$$

The proposed scaling laws are only for estimating the support structure stiffness and radial clearance, and do not provide information about the theoretical limiting load capacity proposed by [9] of specific bearing, because the theory is valid only for isothermal assumption. Reynolds equation based on the continuum theory breaks down once the film thickness approaches the scale of molecular mean free path (MMFP). The increase in static loading is accompanied by decrease in film thickness and corresponding increase in film temperature due to viscous dissipation. The MMFP increases with increasing temperature. Therefore, the thermal effects cause the Reynolds equation to break down at a higher film thickness. In summary, the scaling laws are based on matching the analytical load capacity with the experimental guideline from Eq. (1). Therefore, it is important to note that the limitations of the load capacity guideline also apply to the developed scaling laws.

2.3 Application of Scaling Laws for Reference System

2.3.1 Turbomachinery geometry

The scaling laws are applied to the 3-pad foil bearing with various diameters up to 300 mm to investigate whether such a large foil bearing can be designed and adopted to practical industrial applications. The first step is to devise a turbomachinery configuration that may represent typical single stage gas turbine rotors as shown in Figure 3, where turbine impeller is made of Ni alloy and rest of the system are made of stainless steel. Assuming L/D = 1, for the nominal bearing size (=journal diameter) of D, the assumptions in Table 1 were applied to estimate the total rotor weight of the turbomachinery components. The turbomachinery system shown in Figure 3 was created using the assumptions in Table 1.

Table 1 Assumptions for estimating turbo-machinery geometry

Shaft inner diameter	Thrust runner inner diameter	Thrust runner outer diameter	Thrust runner thickness	Compressor impeller outer diameter	Shaft length
0.66 D	0.66 D	2.2 D	0.22 D	2.75 D	3.5 D

By suitable scaling of the solid model, the dimensions of all turbomachinery components were obtained for various bearing sizes, and the results of thrust runner outer diameter (OD), impeller diameter and bearing shaft length are tabulated in Table 2.

Table 2 Dimensions and mass of turbo-machinery components

Journal OD [mm]	*Thrust runner OD [mm]*	*Impeller OD [mm]*	*Shaft length [mm]*	*Total rotor mass [kg]*	*Rotor mass per bearing [kg]*	*Average bearing pressure [bar]*
20	44.0	55.0	70.0	0.42	0.21	0.050
50	110.0	137.5	175.0	6.30	3.15	0.122
75	165.0	206.3	262.5	21.22	10.61	0.183
100	220.0	275.0	350.0	50.28	25.14	0.243
150	330.0	412.5	525.0	169.68	84.84	0.365
200	440.0	550.0	700.0	402.22	201.11	0.487
250	550.0	687.5	875.0	785.60	392.80	0.608
300	660.0	825.0	1050.0	1357.52	678.76	0.730

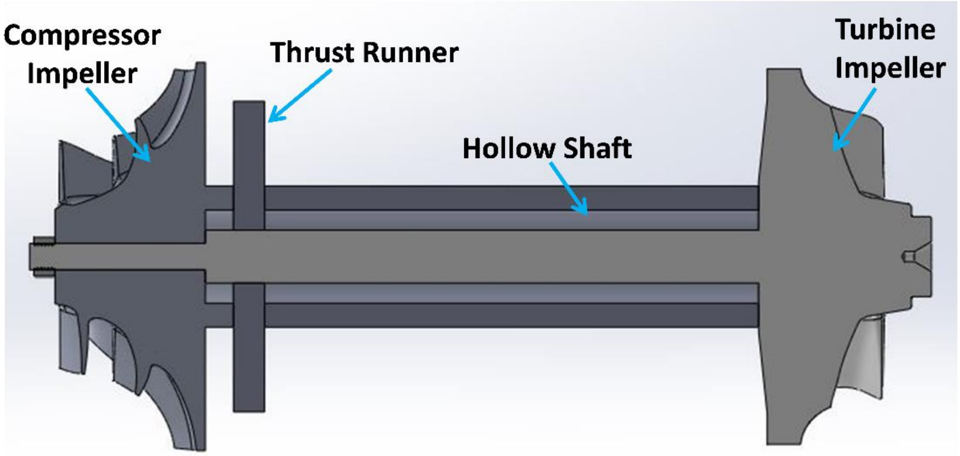

Figure 3 Reference turbomachinery configuration

The mass of individual components and the total load was computed based on the material density of each component. For simplicity, it is assumed two radial bearings support the half of entire rotor weight equally, and the average bearing pressure was calculated by dividing the half of the total rotor weight by the bearing area (D^2). From Table 2, the average bearing pressure is proportional to the bearing diameter while the rotor mass increases with the third power of journal diameter. The solid model is given in a form of single stage gas turbine but the rotor configuration can represent various other oil-free turbomachinery. Typical turbo air blowers use aluminum impellers instead of steel or Ni alloy impellers and the motor is located between the two bearings, compensating the weight reduction at the impellers. For applications using process gas lubricants, Organic Rankine Cycle turbo expanders and refrigerant compressors also use aluminum impellers instead of steel impellers and the motor/generator is located between the two bearings, leading to rather similar rotor weight as the air blowers. Therefore, it is appropriate to use the rotor model in Figure 3 as a representative system for the applicability study of the scaling laws.

2.3.2 Support structure stiffness

The scaling law of support stiffness, Eq. (14) is applicable to any form of support structure. In this paper, corrugated bump foils were chosen as a support structure. For simplicity, it is assumed that the number of bump corrugations is maintained the same regardless of the bearing size (i.e., bump pitch is proportional to the bearing size). Under the assumption of constant number of bumps regardless of the bearing size, the stiffness of individual bump for entire axial length of the bearing will be designed following the scaling law. The assumption of constant number of bumps (pitch scaled to the radius) is a useful tool in the computational domain which simplifies the development of the scaling laws. However, adoption of this assumption leads to too much local sagging of the top foil if the top foil thickness is not altered according to bearing size. Therefore, the practical hardware design implementing the scaling law does not have to follow the same number of bumps. A better implementation of the scaling law for the support structure is through the scaling law of the areal stiffness Eq. (17)

To use the scaling laws for the clearance and bump stiffness, it is important to choose ‘good’ foil bearing as a reference. However, it is not easy to choose specific foil bearing as a reference because all the foil bearings which were successfully integrated to oil-free turbomachinery were designed for certain purpose tailored to its application. Another difficulty is that the detailed design feature of the foil bearings is not usually available. The authors have chosen two foil bearing designs which were successfully applied to oil free-turbomachinery applications. The first design is 21 mm foil bearing developed for 12 kW turbo alternator with rated speed of 140,000 rpm and the second design is 102 mm foil bearing applied to 1000~5000 lbf thrust class oil-free turbine simulator rotor. Both bearings were developed in the authors' laboratory and applied to the intended applications successfully. However, these two bearings are not exactly the same configuration, i.e., number of top foil pads and non-dimensional preload are not identical and number of bump foils are not the same either. To apply the scaling laws for the clearance and bump stiffness, both foil bearings had to be slightly adjusted to use them as common references. Table 3 was created using the scaling laws with the adjusted two bearings as references.

2.3.3 Bearing size and speed

Static and dynamic performances were evaluated for each design in Table 3 for various speeds. Because they are all different in size, the maximum DN number of 3.5 million was applied to find the upper limits of the speed $\left(N_{\max}\right)$ for the various bearing diameters.

The chosen range of DN number ensures almost linear variation of load capacity with speed [8]. The lower bound speeds $\left(N_{\min}\right)$ were assumed to be 20% of the respective $N_{\max}$. Therefore, simulations were conducted for all the cases shown in Table 4. The simulations yielded stiffness and damping coefficients, eccentricity, pressures and film thickness. With the listed clearance and radius combinations, maximum bearing number at $N_{\max}$ is 0.728.

Table 3 Clearance and bump stiffness from scaling laws

Journal OD [mm]	*Clearance [microns]*	*Bump stiffness [MN/m]*	*Areal stiffness [GN/m^3]*
20	54	1.79	68.33
50	85	7.07	43.22
75	104	12.99	35.29
100	120	20.00	30.56
150	147	36.74	24.95
200	170	56.57	21.61
250	190	79.06	19.33
300	208	103.92	17.64

Table 4 Speed data for test cases

Journal OD [mm]	$N_{\min}$					$N_{\max}$
20	35000	63000	91000	119000	147000	175000
50	14000	25200	36400	47600	58800	70000
75	9333	16800	24267	31733	39200	46667
100	7000	12600	18200	23800	29400	35000
150	4667	8400	12133	15867	19600	23333
200	3500	6300	9100	11900	14700	17500
250	2800	5040	7280	9520	11760	14000
300	2333	4200	6067	7934	9800	11667

For all the bearing sizes (journal OD), lift off speeds are expected to be lower than the corresponding $N_{\min}$ because steady state solution for pressure and film thickness could be found for all the cases. As for reference, the lift off speed of aforementioned actual 21 mm foil bearing developed for 12 kW turbo alternator was measured at around 14,000 rpm for actual rotor mass of 0.22 kg per bearing.

2.3.4 Time domain analyses results

Simulation results for bearings following the proposed scaling laws are presented in this section for various shaft sizes. Time domain analysis involves simultaneous solutions for the unsteady Reynolds equation, the journal orbit, and the foil structural deflections. The mathematical details of the solution procedure follow Ref. [22]. The non-dimensional preload of the pad is 0.6 and the pivot offset is assumed to be 0.5. The model for bump dynamics uses a structural loss factor of 0.20. All the simulations were performed at isothermal condition with temperature $50^{o}C$ and air viscosity calculated at the same temperature. The variation of eccentricity with normalized speed (non-dimensionalized by $N_{\max}$) for various bearing sizes is shown in Figure 4 . The pressure and film thickness profiles are shown in Figure 5 to Figure 8. The film thickness normalized by corresponding clearance of each bearing is shown in Figure 9 and Figure 10. The peak pressure increases with bearing size while the minimum film thickness values decrease with increasing bearing size as tabulated in Table 5.

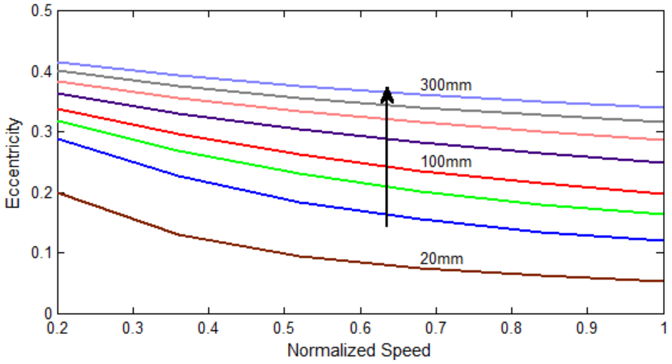

Figure 4 Eccentricity versus normalized speed

The synchronous stiffness and damping coefficients are shown in Figure 11-Figure 14, in which the speeds are normalized with respect to $N_{\max}$ for each bearing size. The direct stiffness increases with the size of the bearing as expected in Figure 11 and Figure 12. However, the variations of k_{xx} with normalized speed for the various bearing sizes show different trends as in Figure 11.

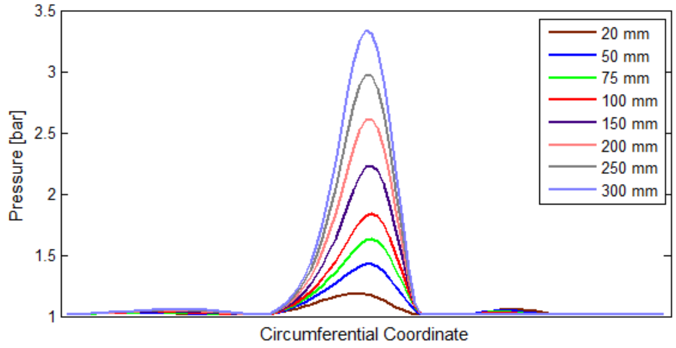

Figure 5 Pressure profile for $N_{\min}$

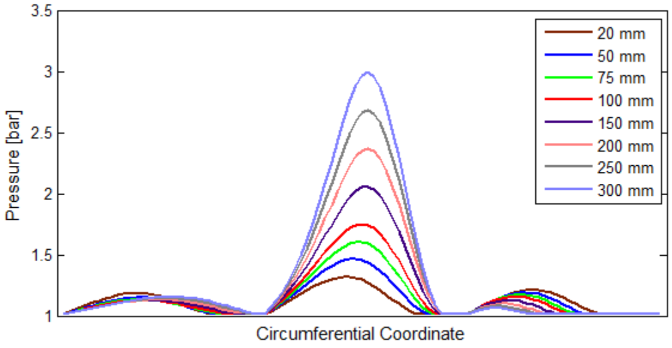

Figure 6 Pressure profile for $N_{\max}$

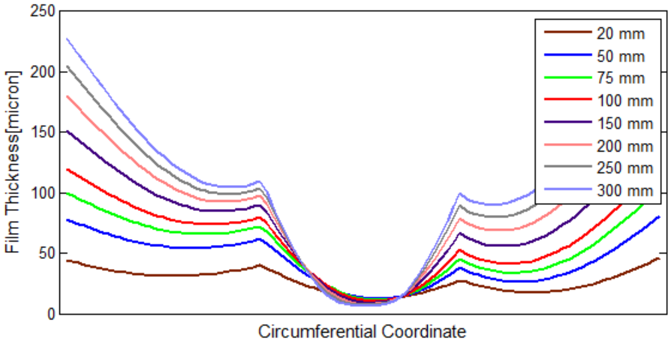

Figure 7 Film Thickness at bearing edge for $N_{\min}$

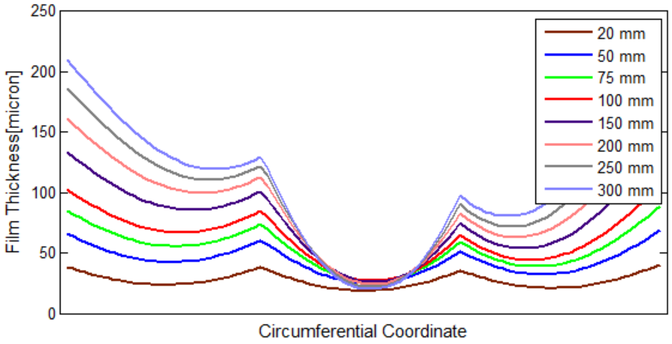

Figure 8 Film Thickness at bearing edge for $N_{\max}$

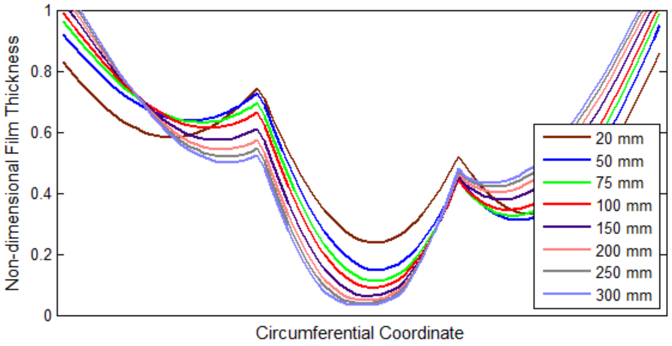

Figure 9 Non-dimensional film thickness at bearing edge for $N_{\min}$

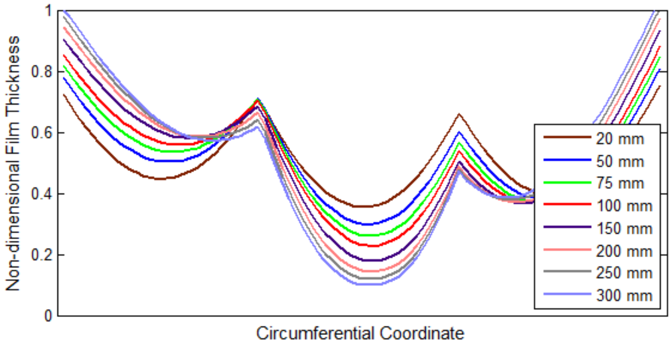

Figure 10 Non-dimensional film thickness at bearing edge for $N_{\max}$

Table 5 Maximum pressure and minimum film thickness

Journal OD [mm]	*Speed [rpm]*	*H_min [micron]*	*P_max [bar]*	*Journal OD [mm]*	*Speed [rpm]*	*H_min [micron]*	*P_max [bar]*
20	35000	12.9	1.19	150	4667	9.4	2.24
	63000	15.9	1.21		8400	14.4	2.15
	91000	17.4	1.24		12133	18.4	2.11
	119000	18.2	1.27		15867	21.5	2.08
	147000	18.8	1.29		19600	24.2	2.07
	175000	19.1	1.32		23333	26.4	2.06
50	14000	12.7	1.43	200	3500	8.2	2.62
	25200	17.7	1.41		6300	12.8	2.51
	36400	20.8	1.42		9100	16.5	2.46
	47600	22.9	1.44		11900	19.6	2.42
	58800	24.4	1.45		14700	22.3	2.39
	70000	25.4	1.47		17500	24.5	2.37
75	9333	11.8	1.64	250	2800	7.4	2.98
	16800	17.2	1.60		5040	11.4	2.86
	24267	20.9	1.59		7280	14.9	2.79
	31733	23.6	1.59		9520	17.8	2.75
	39200	25.6	1.6		11760	20.4	2.71
	46667	27.1	1.61		14000	22.6	2.69
100	7000	10.9	1.84	300	2333	6.8	3.34
	12600	16.3	1.78		4200	10.4	3.2
	18200	20.3	1.76		6067	13.5	3.13
	23800	23.3	1.75		7934	16.2	3.07
	29400	25.6	1.75		9800	18.6	3.03
	35000	27.5	1.76		11667	20.7	3.00

For small bearings, both k_{xx} and k_{yy} increase with shaft speed. However, for large bearings, k_{xx} slightly decreases with speed. This phenomenon can be explained by considering that the total stiffness of the bearing is a net stiffness of the gas film and the bump structural stiffness in series. While the total bump structural stiffness remains constant over a range of speeds for the given bearing size, the film pressure changes with shaft speed. For 300 mm diameter bearing, for example, increase in shaft speed results in increased film thickness (204% increase from $N_{\min}$ to $N_{\max}$) and corresponding reduction in eccentricity shown in Figure 4. The increased film thickness accompanies reduction in the maximum peak film pressure as shown in Table 5 thereby reducing the film stiffness.

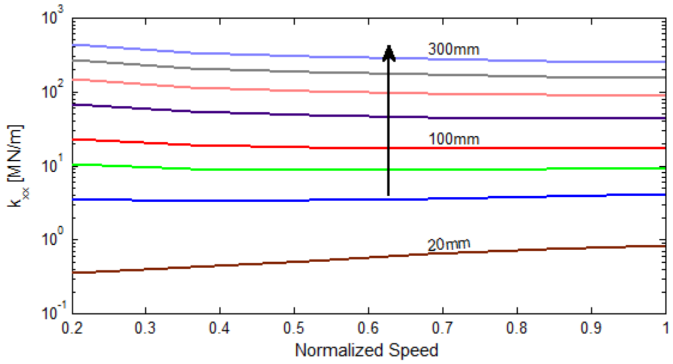

Figure 11 k_{xx} versus normalized speed

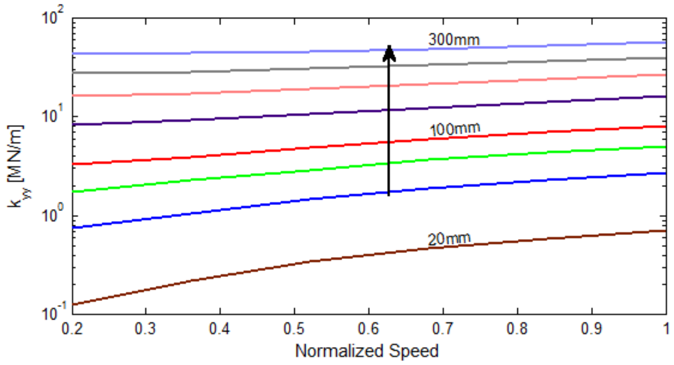

Figure 12 k_{yy} versus normalized speed

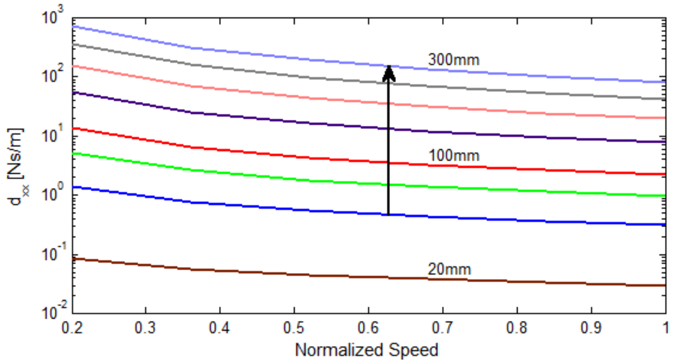

Figure 13 d_{xx} versus normalized speed

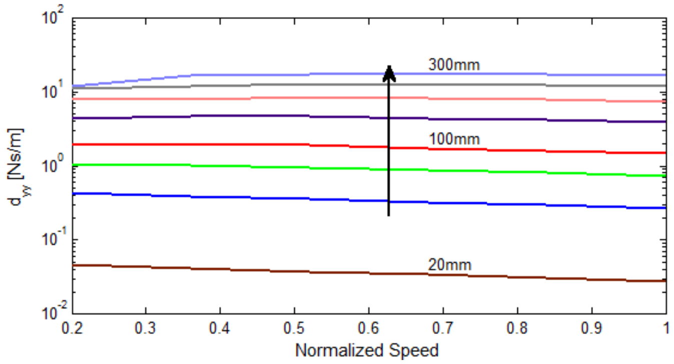

Figure 14 d_{yy} versus normalized speed

For the smallest bearing, however, gas film thickness increases with speed too but the minimum film thickness at $N_{\max}$ is only 48% more than that at $N_{\min}$. Thus, the maximum peak pressure increases with speed. The bearing stiffness is consequently dominated by the gas film resulting in increasing stiffness with speed. The k_{yy} values, though smaller, are of the same order of magnitude as k_{xx} for small sized bearings. However, for larger bearings, the k_{yy} values are an order of magnitude smaller than the k_{xx} due to higher vertical loading. This anisotropic stiffness results in non-circular orbits of the shaft and is beneficial in terms of stability [23]. The k_{yy} value increases substantially with speed (470% increases from $N_{\min}$) for small sized bearings, whereas the corresponding increase in large sized bearings is much smaller (30% increase from $N_{\min}$). The stiffness characteristics once again depend on speed and loading which affect the film thickness and pressure profiles. The direct damping coefficients, d_{xx} and d_{yy}, increase with size as expected Figure 13 and Figure 14. From Figure 13, it is observed that d_{xx} decreases with increasing the shaft speed due to stiffening effect of gas film. However, as the shaft speed is increased, the direct damping d_{yy} slightly decreases except for the large bearings (over 100 mm), where, d_{yy} shows the maximum values in intermediate speeds as shown in Figure 14.

The relative magnitude of cross coupled stiffness compared to the direct stiffness and direct damping is a measure of instability of rotor-bearing systems in general [24]. As shown in Figure 15 to Figure 20, the direct stiffnesses are of the same order of magnitude as the cross-coupled stiffnesses in small sized bearings. However, the relative magnitude of cross-coupled stiffness decreases with the bearing size, which is accompanied by stronger anisotropic behavior of the direct stiffnesses as the bearing size increases.

Centrifugal expansion of the shaft and relative thermal expansion of the shaft with respect to the bearing decrease the local film thickness (and effective clearance) thereby affecting the static and dynamic performance. In foil bearings, thermal expansion of foil structures is negligible compared to those of bearing journal and bearing sleeve. The relative thermal growth of the shaft with respect to the bearing sleeve can be maintained very small if their individual thermal growths are similar. This could be done by appropriate selection of materials and fine tuning the design of bearing sleeve and surrounding structures from a thermal standpoint. Once the thermal effects are addressed by proper thermal management, the local film thickness becomes a function of only the nominal assembly clearance, centrifugal growth, shaft position and the bump deflection. The centrifugal expansion of the hollow shaft under plane stress model [25] is given by

$$r_{cg} = D\frac{\pi^2 \rho (DN)^2}{28800E}[2.3068 - 0.5644\nu] \tag{18}$$

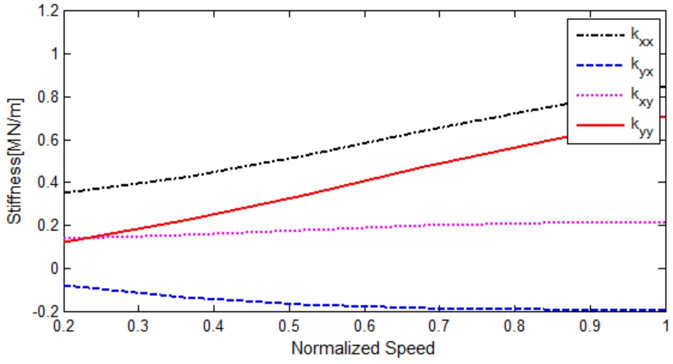

Figure 15 Stiffness components for 20 mm bearing

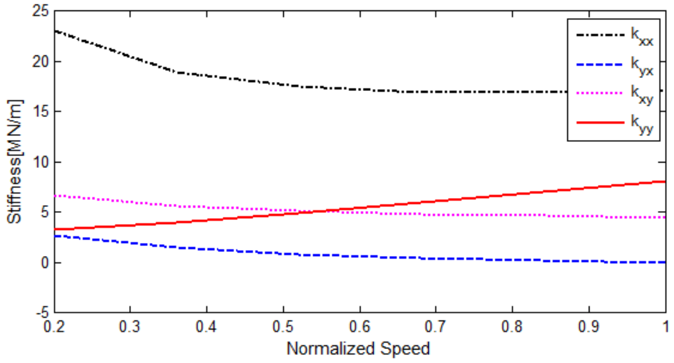

Figure 16 Stiffness components for 100 mm bearing

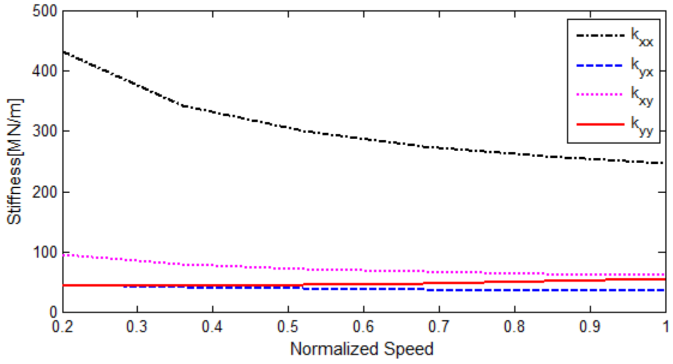

Figure 17 Stiffness components for 300 mm bearing

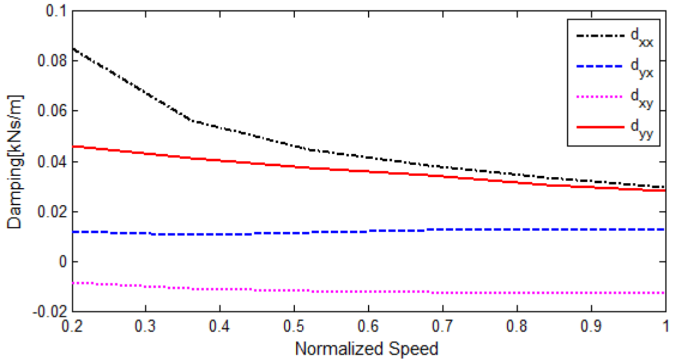

Figure 18 Damping components for 20 mm bearing

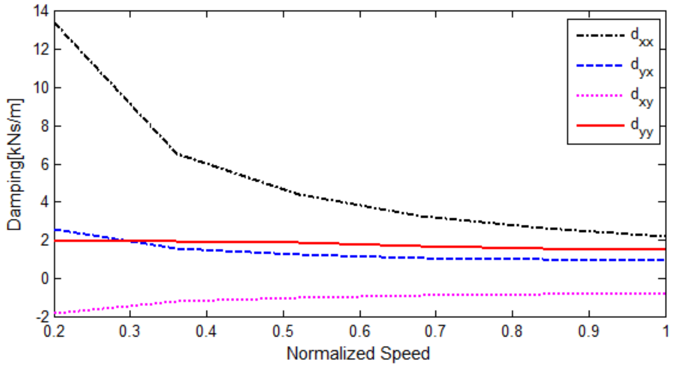

Figure 19 Damping components for 100 mm bearing

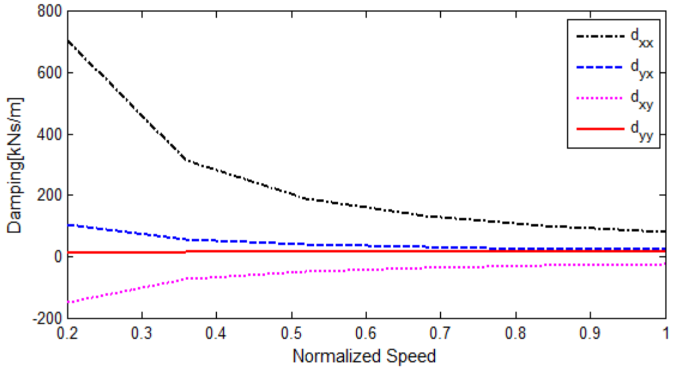

Figure 20 Damping components for 300 mm bearing

2.3.5 Scaling laws as bearing design tool

Scaling laws for radial foil bearings were developed using the scale invariant Reynolds equation and the empirical NASA guideline for load capacity estimation. The first scaling law of the clearance shows that the nominal operating clearance has to be proportional to the square root of the bearing radius. Similarly, a power law relationship between the support structure stiffness and the bearing radius was derived, and it was found that support structure stiffness has to be chosen to be proportional to the bearing radius to the power of 1.5. The implication of these scaling laws is that the preliminary support structure stiffness and nominal clearance for radial foil bearings can be designed without resorting to detailed calculations. These laws serve as a guideline for foil bearing designers in quick choice of initial design parameters. Detailed design of the clearance and support structure stiffness for specific applications requires high level analyses of the bearing characteristics in actual operating conditions. In addition, rotordynamic stability of the foil bearing-rotor systems depends not only on the bearing itself but also on detailed inertia distribution of the rotor.

Chapter 3

4-DOF ROTORDYNAMIC ANALYSIS

3.1 System Configuration for Rotordynamic Analyses

Many of the details presented in this chapter may also be found in Ref. [26]. In small bearings, the magnitudes of the direct and cross coupled stiffness are comparable. At high speeds, the cross coupled forces become significant and could lead to instability. However, in large bearings, the static eccentricity tends to be very large. Consequently, the direct stiffness is much more dominant than the cross coupled components. Instability in these cases may be driven by other mechanisms related to inertia distribution of the rotor.

The turbomachinery configuration considered in the Ref. [3] uses a compressor-turbine system connected by a hollow shaft and it is supported by two preloaded three pad radial foil bearings. When the motion in axial direction is not considered, such a configuration results in 4-DOF motion of the rotor (assuming the first bending mode of the entire rotor is at much higher frequency than the maximum speed) because the system is supported by two radial bearings.

In this study, while the details of the foil bearings are the same as in Ref. [3] (50% offset, 0.6 non-dimensional hydrodynamic preload) the turbomachinery system has been slightly modified to reflect more realistic component sizes, material properties and mass distribution, and it is shown in Figure 21. The turbine impeller material is assumed to be nickel alloy while the compressor is assumed to be made of stainless steel.

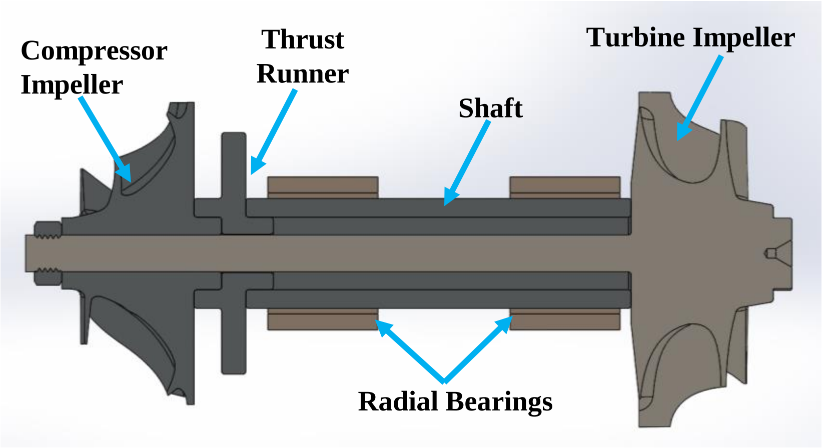

Figure 21 Sectional view of turbomachinery system

Table 6 presents the turbomachinery geometry and the inertia properties. The locations (coordinates) of bearings and the imbalance from rotor mass center of gravity are summarized in Table 7. The bearing clearance and support structure stiffness calculated using Eq. (8) and (15) are presented in Table 8

Table 6 Turbomachinery design data

Journal OD [mm]	150.0	200.0	250.0	300.0
Compressor OD [mm]	412.5	550.0	687.5	825.0
Turbine OD [mm]	476.0	634.7	793.3	952.0
Thrust runner OD [mm]	330.0	440.0	550.0	660.0
Shaft length [mm]	525.0	700.0	875.0	1050.0
Rotor mass, m_r [kg]	205.5	487.0	951.2	1643.6
I_P [kg-m^2]	1.9	8.0	24.4	60.8
I_T [kg-m^2]	21.1	89.0	271.6	675.8

Table 7 Axial locations of the bearings and imbalance from CG

Journal OD [mm]	150	200	250	300
Bearing 1 [mm]	-146.3	-195.1	-243.9	-292.7
Bearing 2 [mm]	176.2	234.9	293.6	352.4
Imbalance 1, l_1 [mm]	-306.8	-409.1	-511.4	-613.7
Imbalance 2, l_2 [mm]	288.7	384.9	481.1	566.4
$u_1 = u_2$ [g-mm]	106.6	341.9	811.0	1634.9

.

Table 8 Clearance and bump stiffness from Ref. [3]

Journal OD [mm]	Bearing Clearance [micron]	Bump Stiffness [MN/m]	Areal Stiffness [GN/m^3]
150	147	36.74	24.95
200	170	56.57	21.61
250	190	79.06	19.33
300	208	103.92	17.64

3.2 Mathematical Formulation

This section presents the pertinent equations for numerical simulation of the turbomachinery system. The coordinate system and the variables describing rotor motions used for simulations are shown in Figure 21.

The equations of cylindrical and conical motions of the rotor are given by Eq. (19) and Eq. (20):

$$\begin{aligned} m_r \ddot{X}_X &= F_{X\_B} + F_{X\_I} + m_r g \\ m_r \ddot{X}_Y &= F_{Y\_B} + F_{Y\_I} \end{aligned} \tag{19}$$

$$\begin{aligned} I_T \ddot{\xi} + I_P \omega \dot{\psi} &= M_{\xi\_B} + M_{\xi\_I} \\ I_T \ddot{\psi} - I_P \omega \dot{\xi} &= M_{\psi\_B} + M_{\psi\_I} \end{aligned} \tag{20}$$

In Eq. (19), the rotor motions in cylindrical mode are represented by X and Y while the mass of the rotor is represented by m_r. In Eq. (20), the transverse and polar moments of inertia of the rotor are I_T and I_P. $F_{X\_B}, F_{Y\_B}, M_{\xi\_B}, M_{\psi\_B}$ are the reaction forces and moments from the journal bearings and $F_{X\_I}, F_{Y\_I}, M_{\xi\_I}, M_{\psi\_I}$ are the forces and moments induced by imbalance mass on the rotor. The imbalance forces and moments are calculated using Eqs. (21) and (22):

$$F_{X\_I}\vec{i} + F_{Y\_I}\vec{j} = \omega^2 \sum_{i=1,2} \left[u_i \cos(\omega t + \phi_i)\vec{i} + u_i \sin(\omega t + \phi_i)\vec{j} \right] \tag{21}$$

$$M_{X\_I}\vec{i} + M_{Y\_I}\vec{j} = \sum_{i=1,2} l_i \vec{k} \times \left(F_{X\_I}\vec{i} + F_{Y\_I}\vec{j} \right) \tag{22}$$

where, i, j and k are unit vectors corresponding to radial $\left(X,Y\right)$ and axial $\left(Z\right)$ directions, respectively, $u_{i=1,2}$ are the imbalance amount and $l_{i=1,2}$ are the axial location of the imbalance from the center of mass of the system. The bearing reaction forces and moments are calculated using Eqs. (23) and (24):

$$F_{X\_B}\vec{i} + F_{Y\_B}\vec{j} = \sum_{j=1,2} \iint d\vec{F}_{Bj} \tag{23}$$

$$M_{\xi\_B}\vec{i} + M_{\psi\_B}\vec{j} = \sum_{j=1,2} \iint Z\vec{k} \times d\vec{F}_{Bj} \tag{24}$$

where, $d\vec{F}_{Bj} = p_j\left(\cos\theta\vec{i} + \sin\theta\vec{j}\right)Rd\theta \cdot dZ$. The axial coordinate Z in Eq. (25) is related to local bearing coordinate z_{bj} and axial locations of the bearings Z_j with respect to the mass center of the system through:

$$Z = Z_j - L/2 + z_{bj} \tag{25}$$

Where, L is the length of each bearing as shown in Figure 23. The local pressure in each bearing is calculated by solving transient Reynolds equation applied to each bearing:

$$\begin{aligned} &\frac{\partial}{R^2\partial\theta}\left(ph^3\frac{\partial p}{\partial\theta}\right)_j + \frac{\partial}{\partial z_b}\left(ph^3\frac{\partial p}{\partial z_b}\right)_j \\ &= 6\mu\omega\frac{\partial}{\partial\theta}\left(ph\right)_j + 12\mu\frac{\partial}{\partial t}\left(ph\right)_j,\ j = 1,2 \end{aligned} \tag{26}$$

The film thickness distribution in the bearing depends on the operating clearance, shaft motion, and local deflection and is given by:

$$h_j(\theta, z_{bj}) = C + \left(X + \psi Z_j\right)\cos\theta + \left(Y - \xi Z_j\right)\sin\theta + \delta_j\left(\theta, z_{bj}\right) \tag{27}$$

The foil deflection $\delta_j\left(\theta, z_{bj}\right)$, follows independent elastic foundation model.

3.3 Simulation Results for 4-DOF Turbomachinery System

3.3.1 Rotordynamics behavior

The results of rotordynamic simulations for turbomachinery with large bearings designed following the scaling laws for radial clearance and support structure stiffness are presented in this section. The maximum speed in each case was limited to DN of 3.5 million.

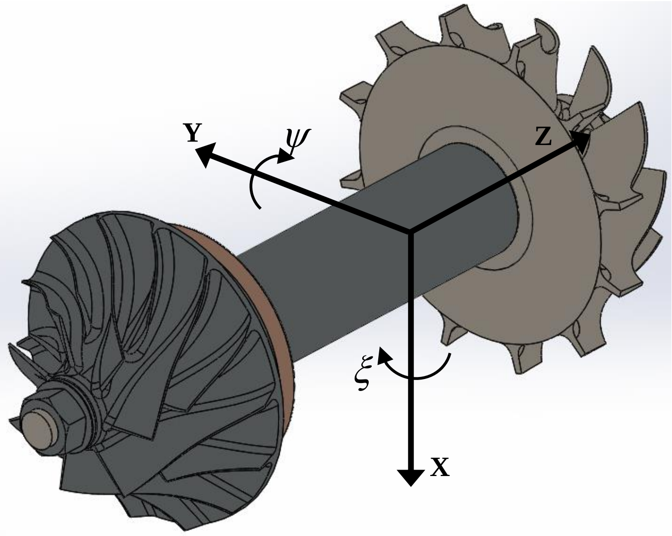

Figure 22 Coordinate system for 4DOF motions

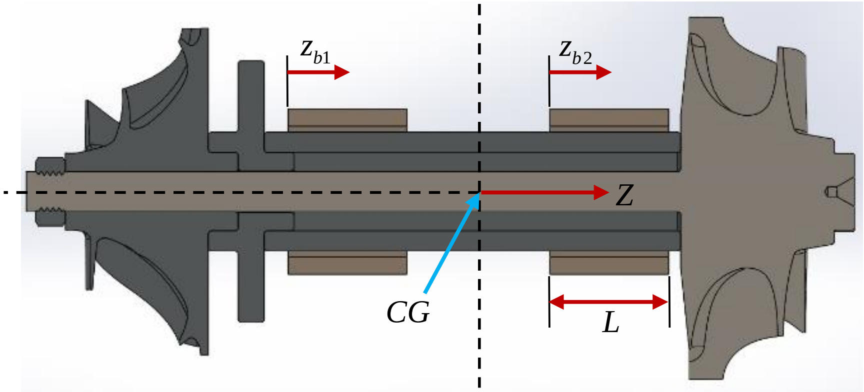

Figure 23 Details of axial coordinate system

In the simulations, cylindrical mode is excited by setting and conical mode is excited by setting . The waterfall plots for vibrations (in X direction) at the 1st bearing (located next to the thrust runner) are presented in Figure 24-Figure 31. The conical mode vibrations can be seen in Figure 24-Figure 27while the cylindrical mode vibrations can be seen in Figure 28-Figure 31 for the various bearing sizes.

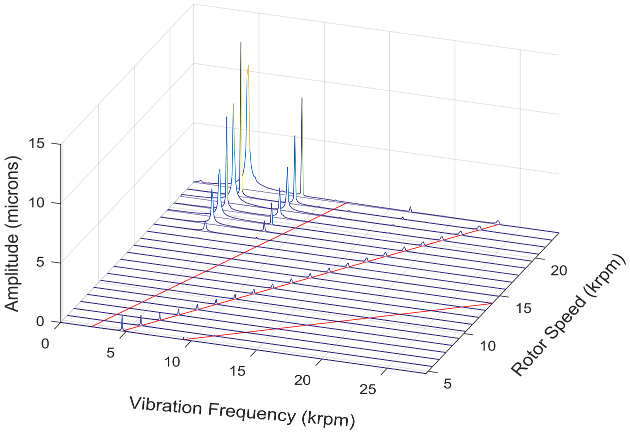

Figure 24 Waterfall plot for conical mode at 1st bearing for 150 mm bearing

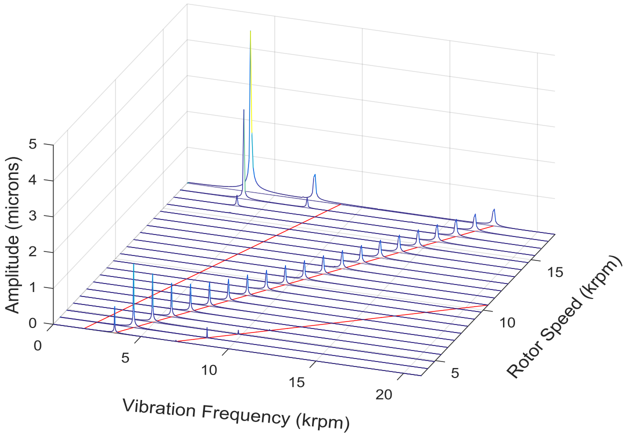

Figure 25 Waterfall plot for conical mode at 1st bearing for 200 mm bearing

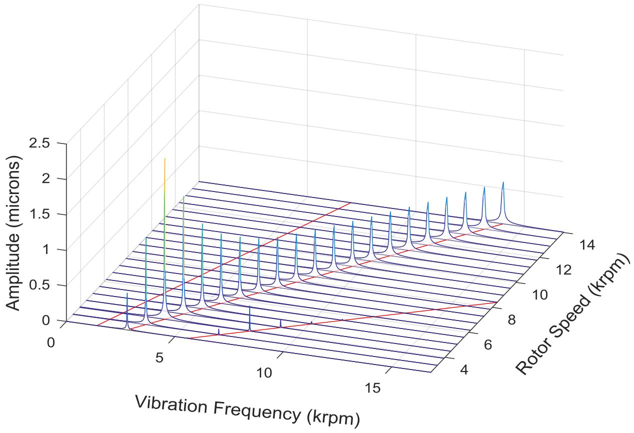

Figure 26 Waterfall plot for conical mode at 1st bearing for 250 mm bearing

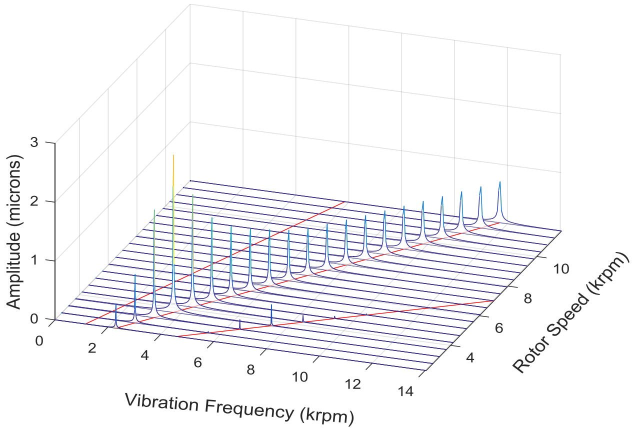

Figure 27 Waterfall plot for conical mode at 1st bearing for 300 mm bearing

The synchronous vibrations increase with bearing sizes but critical speed remains almost the same for both conical mode (around 4,000rpm) and cylindrical mode (around 8,000rpm). For the 150mm bearing, the magnitudes of sub-synchronous vibrations are large as shown in Figure 24 and Figure 28. In contrast, the sub-synchronous vibrations are not present for 250mm and 300mm bearings as shown in Figure 26, Figure 27, Figure 30, and Figure 31. Harmonics of sub-synchronous vibrations can be also seen, which is typical for non-linear systems. One of the strategies for mitigating the sub-synchronous vibrations and improving the rotordynamic stability for 150 and 200mm bearings would be through increasing the preload as suggested by Ref. [27, 28] or adjusting clearance and bump stiffness.

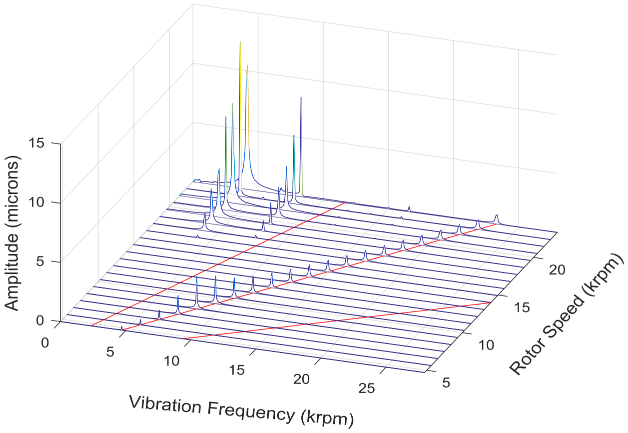

Figure 28 Waterfall plot for cylindrical mode at 1st bearing for 150 mm bearing

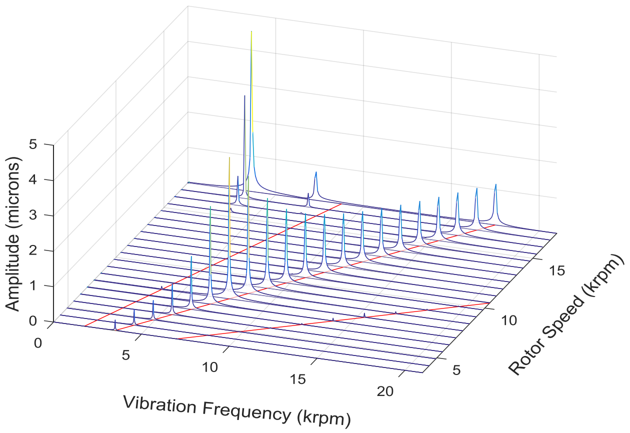

Figure 29 Waterfall plot for cylindrical mode at 1st bearing for 200 mm bearing

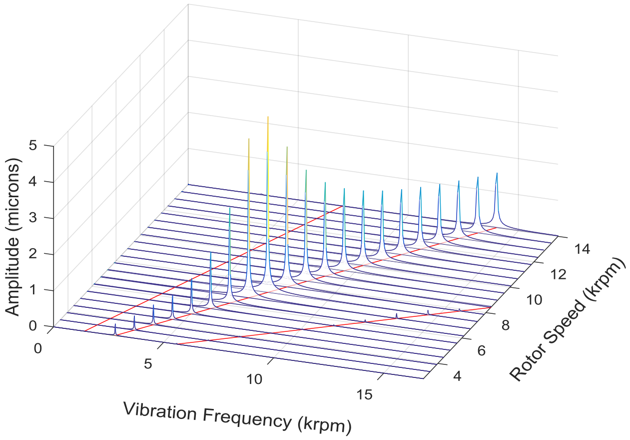

Figure 30 Waterfall plot for cylindrical mode at 1st bearing for 250 mm bearing

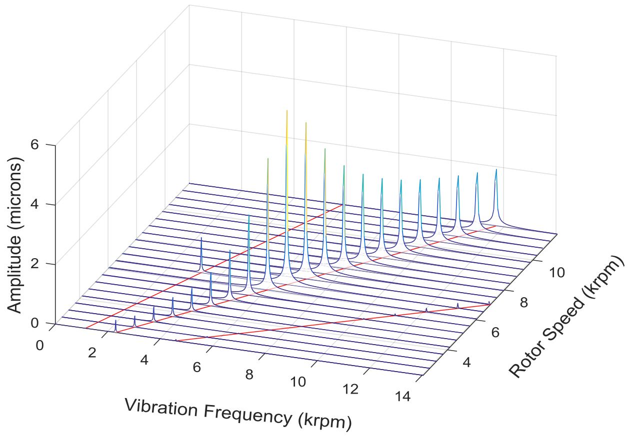

Figure 31 Waterfall plot for cylindrical mode at 1st bearing for 300 mm bearing

General trend of critical speeds appearing in the waterfall plots is more clear in the Bode plot for the various bearing sizes with non-dimensional speed (normalized with maximum speed, i.e., DN 3.5 million) in the abscissa as shown in Figure 32 and Figure 33.

The critical speeds are functions of system characteristics such as stiffness, damping and inertia.

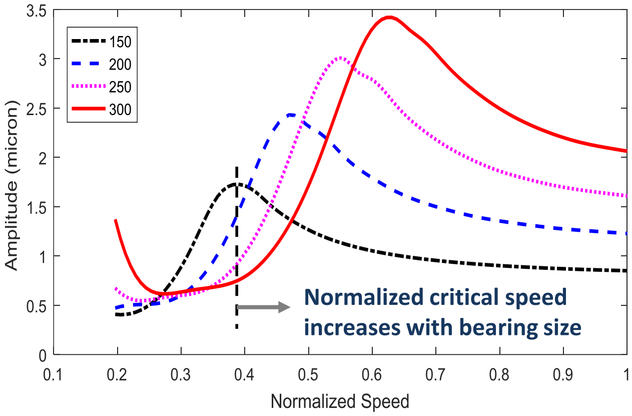

Figure 32 Bode plot for cylindrical mode

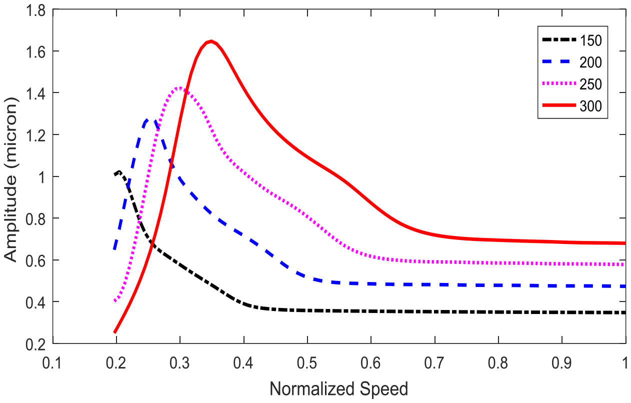

Figure 33 Bode plot for conical mode

In the turbomachinery system shown in Figure 21, while the mass increases with the third power of bearing size, the mass moment of inertia increases as the fifth power of bearing size. The general trend of stiffness and damping coefficients are more difficult to find but they both increase in non-linear fashion with respect to the bearing size as presented in Ref. [3]. Actual critical speeds for the different bearing sizes appear at speed around 8,000 rpm regardless of the bearing size as shown in Figure 24-Figure 27. However, the normalized critical speed (actual critical speed divided by the maximum speed of each case) increases almost linearly with the bearing size. The better rotordynamic stability of large systems is related to the trend of the normalized critical speed. As the normalized critical speed increases, onset speed of instability also increases in general, and such a trend is clearly visible in the analyses.

From these figures, the general trend indicates that the stability of the turbomachinery configuration increases as the system is scaled up to larger bearing sizes which indicates that the increased static loading (increased mass) sufficiently enhances the stability despite increase in moment of inertia. More detailed insight to the reason for the enhanced stability of the large bearing-rotor system can be found from frequency domain modal analyses.

3.3.2 Modal analyses

In rotordynamic analyses, the overall stiffness and damping characteristics of the bearings at certain speed are best described by modal impedance values as a function of excitation frequency. Details of the modal analysis method are presented elsewhere [29]. The real part of the modal impedance corresponds to the modal stiffness while the imaginary part corresponds to damping characteristics. The analysis of the conical modal impedance follows Ref. [29] and the total rotor weight is assumed to be equally distributed between the two bearings though they are not symmetric about the center of mass of the system. However, the double overhung rotor layout shown in Figure 21 renders nearly symmetric loading to the two radial bearings.

Figure 34 and Figure 35 show the impedance plots for conical mode, and Figure 38 shows details of the modal damping below excitation frequency ratios below 0.5. For the 150mm and 200mm bearings, small negative damping is observed but they are positive for most excitation frequency ratios. Especially modal damping for the synchronous excitation (imbalance excitation) is large positive value, which is beneficial to reduce any sub-synchronous vibrations due to low frequency excitations. For 250mm and 300mm bearings, the modal damping is all positive for entire excitation frequency ratio. The impedances for cylindrical mode are shown in Figure 36 and Figure 37, and details of the modal damping below excitation frequency ratio below 0.5 is presented in Figure 39. The modal stiffness values increase with increasing values of excitation frequency. The modal damping is slightly negative for all the bearing sizes but they are relatively small values compared to those at synchronous excitation.

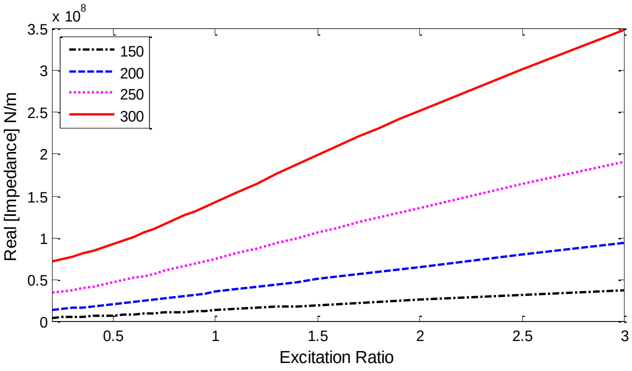

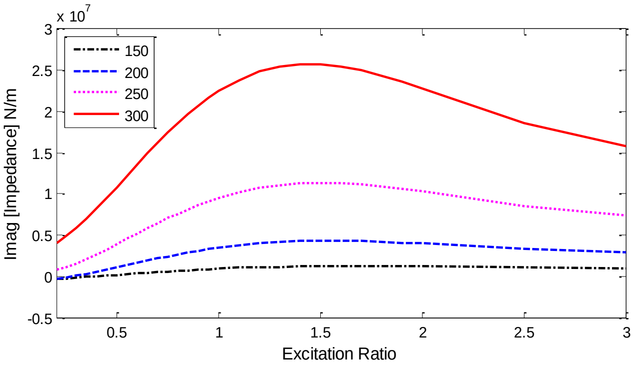

Figure 34 Real part of impedance for conical mode for DN of 3.5×10^6

Figure 35 Imaginary part of impedance for conical mode for DN of 3.5×10^6

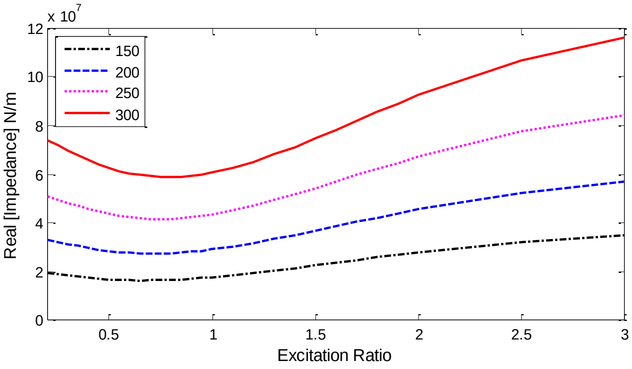

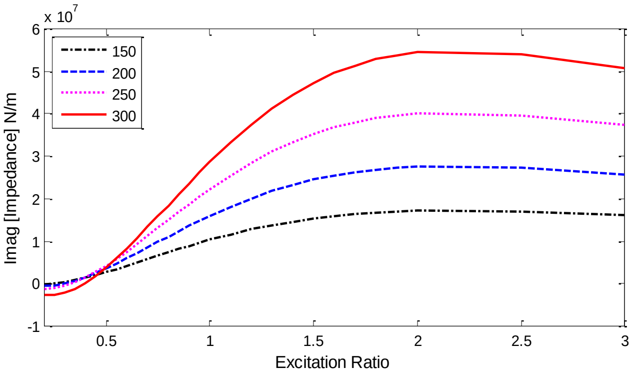

Figure 36 Real part of impedance for cylindrical mode for DN of 3.5×10^6

Figure 37 Imaginary part of impedance for cylindrical mode for DN of 3.5×10^6

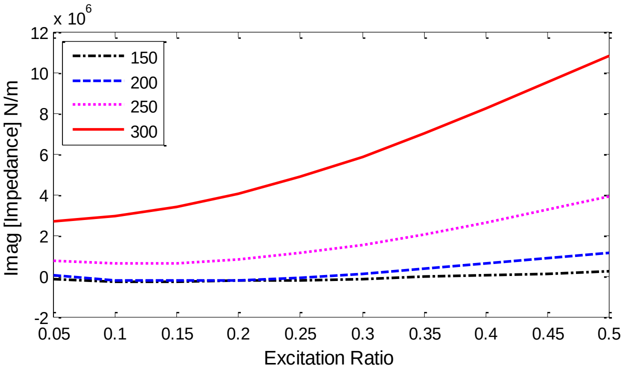

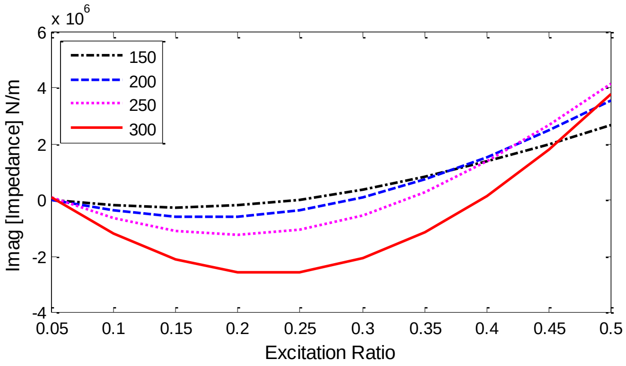

Figure 38 Conical mode modal damping below excitation frequency ratio of 0.5

Figure 39 Cylindrical mode modal damping below excitation frequency ratio of 0.5

From the modal analyses, general trend of rotordynamic stability of the foil bearing-double overhung rotor systems shown in the waterfall plots can be confirmed; larger systems are more stable when the bearings are designed following the scaling laws in Eqs.(9), (15) and(17). It is noteworthy that the bearing designs following these scaling laws are initial design from which fine tuning is further necessary depending on the operating environment and final rotor layouts.

3.4 Case Studies

Assuming the turbomachinery configuration shown in Figure 21 can be configured to a double overhung turbo blower or turbo compressor with high power density permanent magnet motor located between the two wheels, thermo/aerodynamic calculations were performed on the single stage centrifugal compressor wheels of each size to investigate shaft power for each size. The purpose of case studies in this section is to investigate feasibility of megawatt (MW) scale turbo blowers or turbo compressors with foil bearings.

So far the largest commercially available turbo blower with foil bearings is 650hp (487.5 kW). Table 9 presents summary of low-pressure compressor (or blower) with pressure ratio 1.7 (total to total) and Table 10 presents summary of medium pressure compressor with pressure ratio 3.1 (total to total). Figure 40 and Figure 41 represents plots of component sizes vs. shaft power of single compressor wheel. Design point of 1MW blower (500 kW each wheel) and 1.5MW (750 kW each wheel) compressor are highlighted. Realization of such MW oil-free machines is very feasible from the fact that MW scale high speed permanent motors are commercially available.

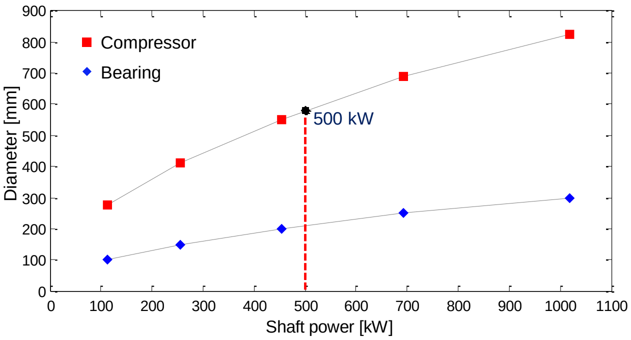

Figure 40 Shaft power of single compressor wheel vs sizes of compressor and bearing, pressure ratio = 1.7

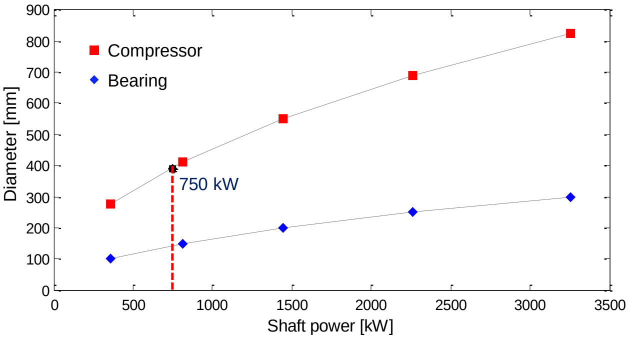

Figure 41 Shaft power of single compressor wheel vs sizes of compressor and bearing, pressure ratio = 3.1

Table 9 Summary of low pressure compressors (Pr=1.7)

Bearing [mm]	Compressor [mm]	Speed [rpm]	Shaft power [kW]	Mass flow rate [kg/s]
100	275.0	20,455	226.6	3.58
150	412.5	13,620	511.0	8.08
200	550.0	10,227	906.4	14.34
250	687.5	8,272	1385.4	21.92
300	825.0	6,818	2039.2	32.26

Table 10 Summary of medium pressure compressors (Pr=3.1)

Bearing [mm]	Compressor [mm]	Speed [rpm]	Shaft power [kW]	Mass flow rate [kg/s]
100	275.0	35,000	723.4	4.92
150	412.5	23,333	1627.8	11.08
200	550.0	17,500	2933.8	19.68
250	687.5	14,000	4521.6	30.76
300	825.0	11,667	6511.0	44.30

Figure 43 presents scale model of 1.5 MW medium pressure compressor (Pr=3.1) with permanent magnet sleeve (shown with actual size from the commercial supplier) located between the two overhung compressors. In the model, bearing journal is 130 mm and compressor wheel is 390 mm and total rotor weight is about 140 kg, and speed is 24,331 rpm, which is close to the speed rate (25,000 rpm) of the motor. It is interesting to note that from Figure 41 or Table 10, 300 mm foil bearings can support a rotor of over 6 MW oil-free single stage compressors. Design and operation of such large foil bearings are challenging during start /stop of the machine because average bearing pressure due to the rotor weight alone is about 90~100 kPa.

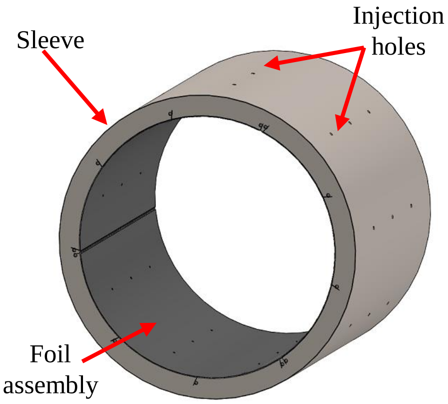

Figure 42 Conceptual design of hybrid foil bearing design

Figure 43 Scale model of 1.5 MW medium pressure compressor with foil bearings

Hybrid foil bearings adopting external pressurization are strong candidates for the realization of such large foil bearings. Typical configuration of hybrid foil bearings is shown in Figure 42. Injection holes are formed on the sleeve directly and there are nine injection holes per pad. However, the number of injection holes can be adjusted for different applications.

Figure 44 and Figure 45 present predicted bearing pressure of 250mm and 300mm hybrid foil bearings with the same clearance and bump stiffness adopted from Table 3 at their lowest speeds presented in Ref.[3]. With 5 bar multi-point injection, minimum clearance of the bearings are over 30 microns under 4,666N (250mm bearing) and 8,062N (300mm bearing), which are half of the total rotor mass. The external pressurization is required during only start-up/stops and it can be turned off or supply pressure can be reduced once full design speeds are reached.

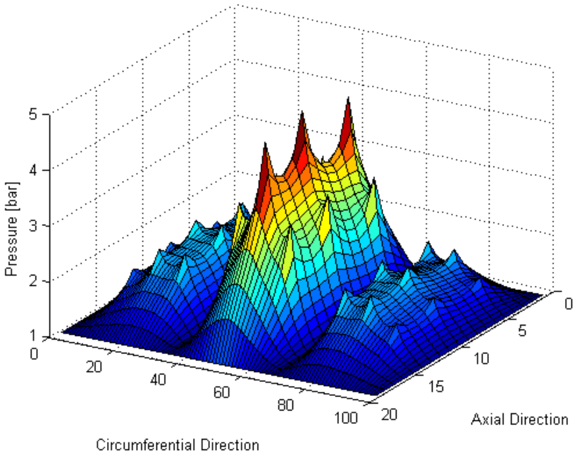

Figure 44 Pressure profile for 250 mm bearing under load of 4666N at lowest speed

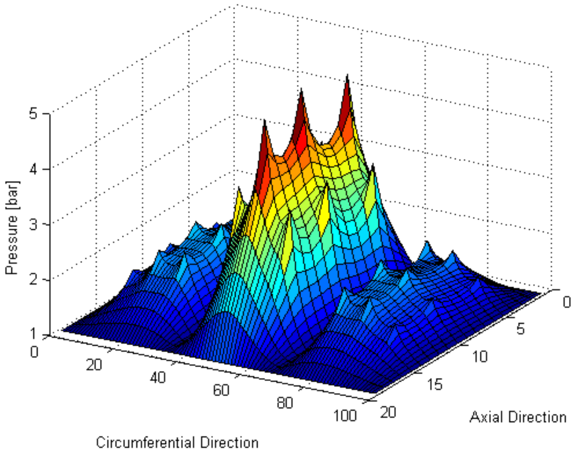

Figure 45 Pressure profile for 300 mm bearing under load of 8062 N at lowest speed

Chapter 4

DESIGN OF LARGE FOIL BEARING

The rotor-dynamic simulation results for turbomachinery systems incorporating foil bearings showed that sub-synchronous vibrations disappear when bearing size increases beyond 250 mm. This effect was attributed to increased vertical loading which has a stabilizing effect. However, there are many factors that must be considered when foil bearings are used for supporting large sized turbomachinery systems.

To elucidate the design process for large bearings, this chapter presents the details of a 200 mm hybrid air foil bearing that was designed following scaling laws for radial clearance and support structure stiffness. Simulations similar to those outlined in the previous chapters are conducted to determine the characteristics of the hybrid bearing. However, the Reynolds equation must be modified as:

$$\frac{\partial}{\partial x}\left(\frac{R\omega}{2}ph-\frac{1}{12\mu}ph^{3}\frac{\partial p}{\partial x}\right)+\frac{\partial}{\partial z}\left(-\frac{1}{12\mu}ph^{3}\frac{\partial p}{\partial z}\right)+\frac{\partial\left(ph\right)}{\partial t}=\frac{RT\dot{m}_{s}}{A_{cont}} \tag{28}$$

where, A_{cont} is the area defined by computational grid points surrounding the orifice. For flow through orifice as an isentropic process, the non-dimensional mass flow rates are of the form:

$$\dot{M}_{s}=\Gamma_{s}P_{s}H\left[\frac{2\kappa}{\kappa-1}\left(\left(\frac{P}{P_{s}}\right)^{2/\kappa}-\left(\frac{P}{P_{s}}\right)^{\kappa+1/\kappa}\right)\right]^{1/2}\quad \text{for}\quad \frac{P}{P_{s}}>\left(\frac{2}{\kappa+1}\right)^{\kappa/(\kappa-1)} \tag{29}$$

$$\dot{M}_{s}=\Gamma_{s}P_{s}H\left[2\frac{\kappa}{\kappa-1}\left(\left(\frac{P}{P_{s}}\right)^{2/\kappa}-\left(\frac{P}{P_{s}}\right)^{\kappa+1/\kappa}\right)\right]^{1/2}\quad \text{for}\quad \frac{P}{P_{s}}<\left(\frac{2}{\kappa+1}\right)^{\kappa/(\kappa-1)} \tag{30}$$

where $\Gamma_{s}=12\mu C_{d}A_{cont}\sqrt{R_{g}T}\,/\,p_{a}C^{3}$ is feed parameter, P_{s} is supply pressure, κ is the ratio of specific heats, and C_{d} is discharge coefficient [30]. The details of the numerical method can be found elsewhere [31]. The results of the simulations are presented in section

4.1. There are several nuances to be considered in the foil bearing development in addition to bearing performance characteristics. The design must also consider the manufacturing aspects of each component. These insights can only be gleaned through rigorous experimentation and fine tuning of design through an iterative process. The design features of 200 mm foil bearing, and the hardware configuration of the bearing and the test rig are discussed in section 4.2 and section 4.3. Finally, the instrumentation for data acquisition, the experimental procedure and the results are discussed.

4.1 Simulation results for 200 mm HAFB

The simulation results for 3 pad HAFB designed following the scaling laws show that adequate load capacity exists with 5 bar multi point injection under 1961 N operating at 1000 rpm as shown Figure 46 and Figure 47. The peaks in the figures indicate orifice locations. Two orifices each are located on each pad at $\theta = 60^\circ, \theta = 180^\circ$ (direction of gravitational loading) and $\theta = 300^\circ$ with a total of 6 orifices for the bearing. The minimum film thickness obtained is 14.5 micron. Simulations were also conducted for the case of hydrostatic injection only from orifices at $\theta = 180^\circ$ (loaded pad) under the same loading and speed conditions as shown in Figure 48 and Figure 49. The minimum film thickness thus obtained is 13.2 micron which still demonstrates adequate load capacity under low operating speed.

As the operating speed increases, the minimum film thickness increases and the eccentricity decreases. Under those conditions, external pressurization may be turned off. When hydrostatic injection is provided only on the loaded pad, the resulting mass flow rate required is significantly reduced.

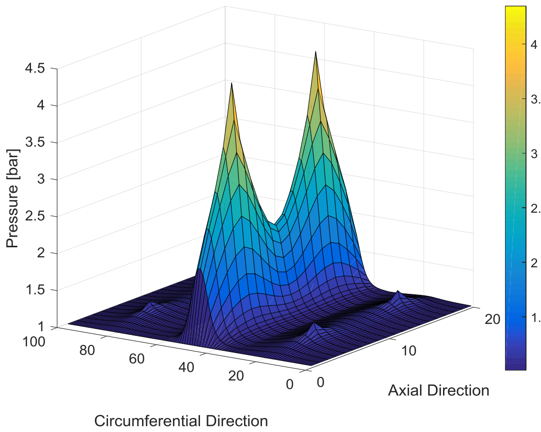

Figure 46 Pressure profile for 200 mm 3 pad HAFB with 5 bar multipoint injection at 1000 rpm under a load of 1961 N

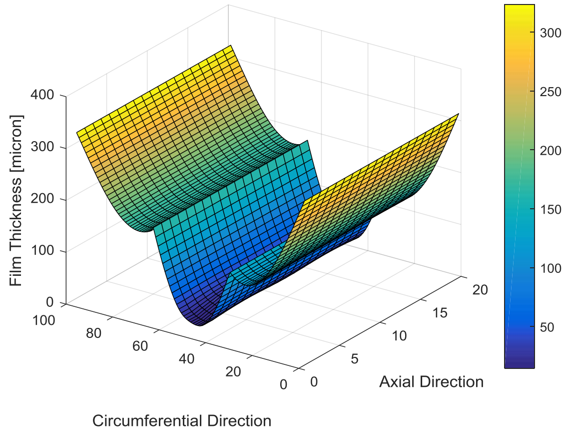

Figure 47 Film thickness distribution for 200 mm 3 pad HAFB with 5 bar multipoint injection at 1000 rpm under a load of 1961 N

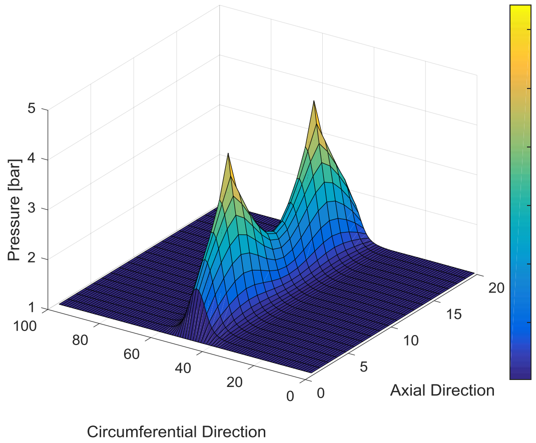

Figure 48 Pressure profile for 5 bar hydrostatic injection only along negative X direction at 1000 rpm under loading of 1961 N

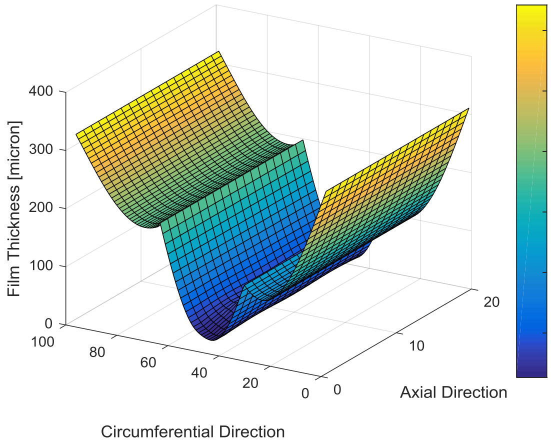

Figure 49 Film thickness distribution for 5 bar hydrostatic injection only along negative X direction at 1000 rpm under loading of 1961 N

The stiffness and damping characteristics for 3 pad hybrid foil bearing under 1961 N operating between 1000 rpm and 18000 rpm with 5 bar multipoint hydrostatic injection from all orifices is shown in Figure 50 and Figure 51. Similar plots are presented for the case of hydrostatic supply only to the loaded pad. The bearing characteristics are a function of interplay between the hydrostatic effects from supplied air and the hydrodynamic effects of the rotating journal. At high speeds, the hydrodynamic effects cause rapid increase in k_{xx}

and k_{yy} as shown in Figure 50 and Figure 52. The stiffness and damping characteristics for the air injection in all orifices and for the case air injection in only loaded pad indicate similar trends.

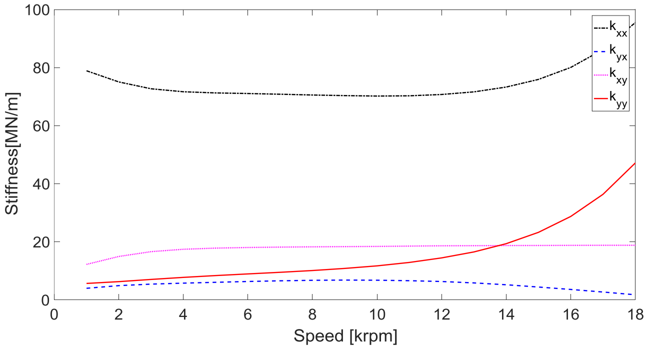

Figure 50 Stiffness components for 200 mm 3 pad HAFB with 5 bar multipoint injection under 1961 N

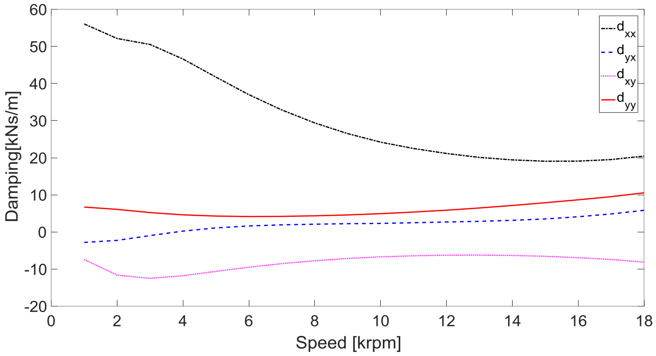

Figure 51 Damping components for 200 mm 3 pad HAFB with 5 bar multipoint injection under 1961 N

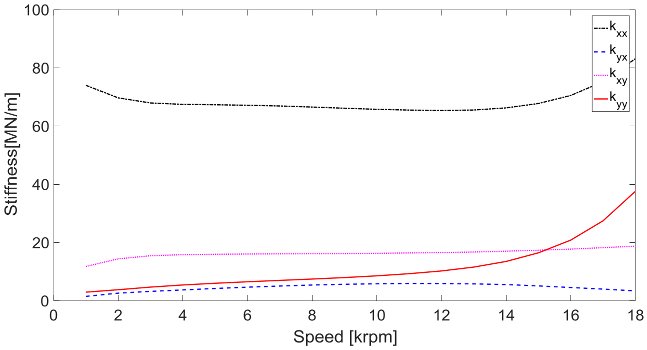

Figure 52 Stiffness components for 200 mm 3 pad HAFB with 5 bar hydrostatic injection only along negative X direction under 1961 N

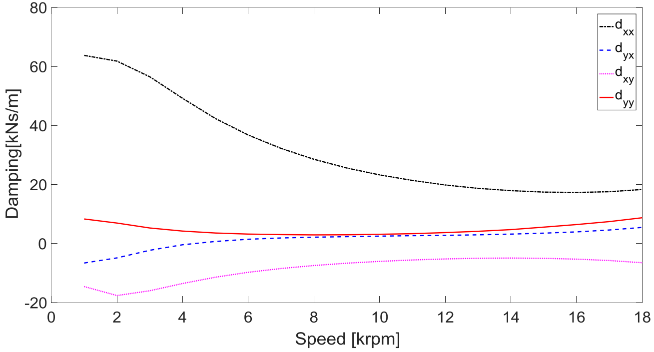

Figure 53 Damping components for 200 mm 3 pad HAFB with 5 bar hydrostatic injection only along negative X direction under 1961 N

For the 3 pad HAFB with pressurized air injection in all pads, it is evident that the synchronous direct stiffness is much higher than the cross coupled stiffness components at high operating speeds as shown in Figure 54 and Figure 55. At subsynchronous excitation, the damping term d_{yx} is positive. However, it decreases in magnitude as excitation frequency ratio increases as seen in Figure 57.

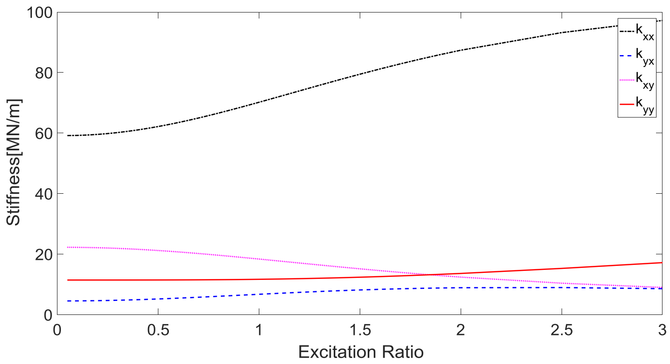

Figure 54 Stiffness versus excitation ratio for 200 mm HAFB at 10 krpm

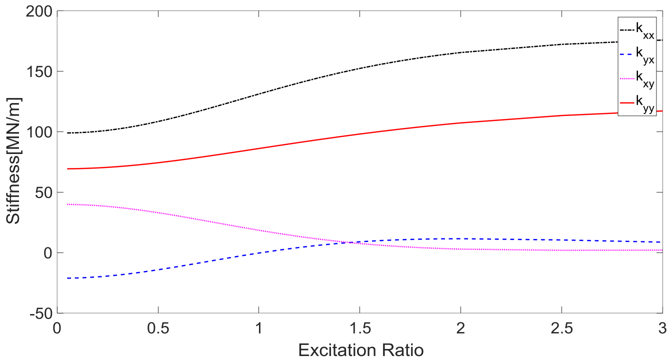

Figure 55 Stiffness versus excitation ratio for 200 mm HAFB at 20 krpm

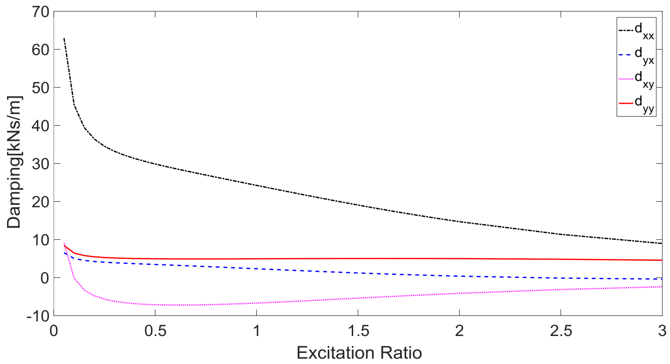

Figure 56 Damping versus excitation ratio for 200 mm HAFB at 10 krpm

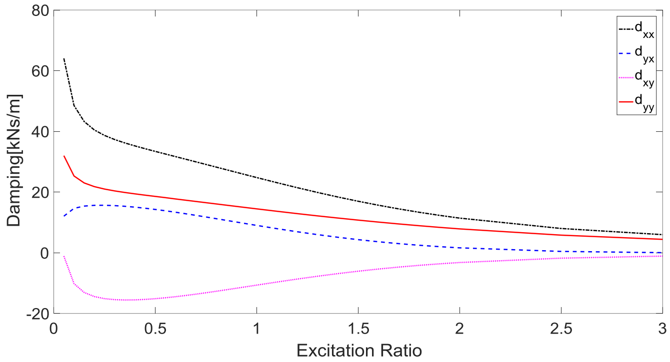

Figure 57 Damping versus excitation ratio for 200 mm HAFB at 20 krpm

4.2 Design of 3 pad HAFB

The 200 mm test bearing designed incorporates 3 sets of top foils and corresponding bump foil assemblies which are all made of Inconel X750. Therefore, the resulting bearing represents 3-pad configuration. The preload for each pad is 180 μm, the pad angle is 115 degrees and the bearing offset is 0.5. Two 2 mm holes are drilled on each top foil 100 mm apart as shown in Figure 58. The bearing sleeve with the attached foils is shown in Figure 59. The bearing clearance and bump stiffness were selected following the scaling laws and actual hardware was designed and provided by Bellkim Energy LLC. The author was involved in the manufacture of the hardware.

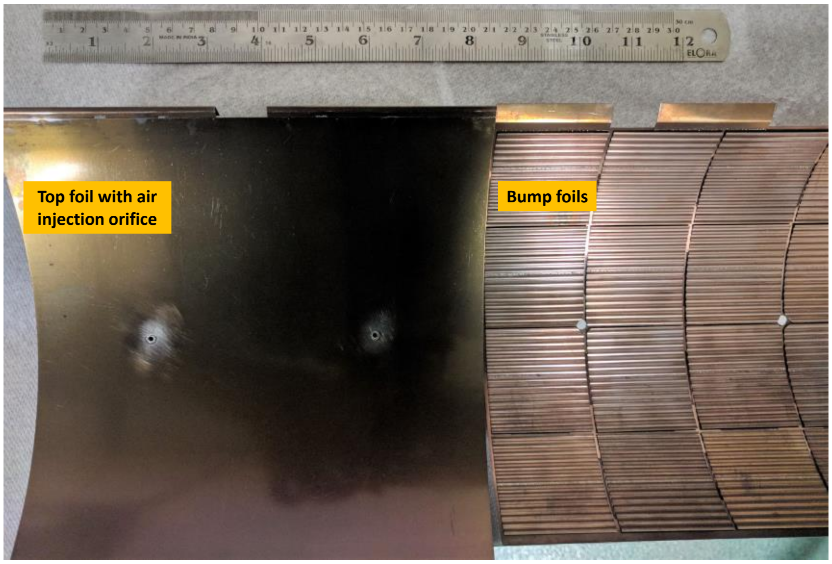

Figure 58 Top foil and bump foil assembly showing injection orifice

Figure 59 Bearing sleeve with foils attached

4.3 Test rig design and construction

A detailed 3-D model of the test set up is shown in Figure 60 and the actual hardware for conducting the experiment is shown in Figure 61. The experimental test set up consists of an induction motor that drives the test journal using a drive shaft supported on 2 sets of duplex ball bearings. The motor is connected to the drive shaft through a flexible coupling which mitigates the effects of minor misalignment.

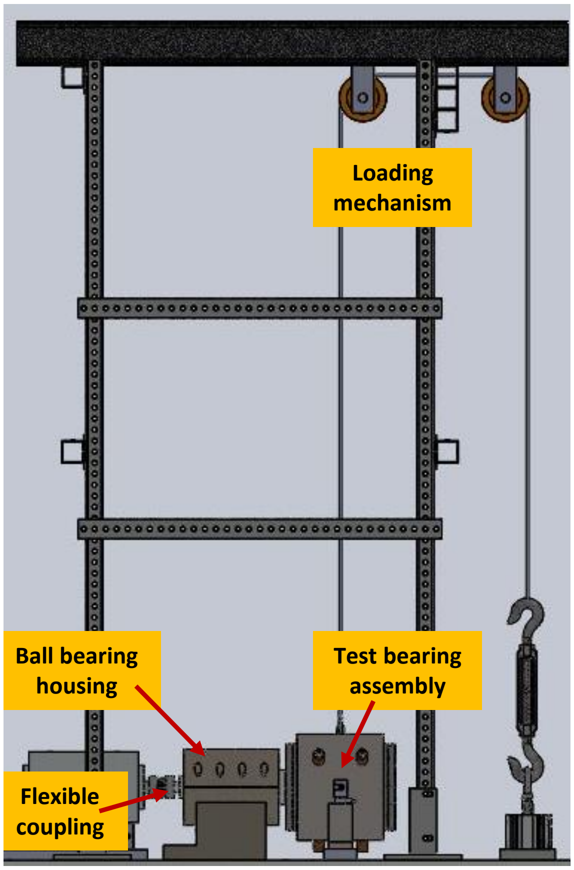

Figure 60 Model of the test rig

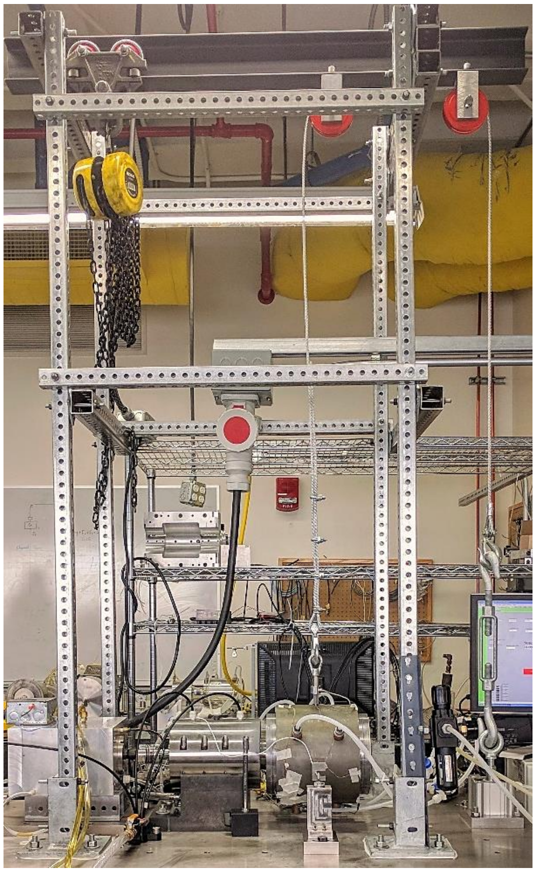

Figure 61 Hardware used for experiment

The drive shaft is rigidly connected to the hollow test journal through one of its end plates. The tension bolt used to connect the drive shaft and the hollow journal is loaded using a specialized puller. The tension bolt is made of 17-4 H900 stainless steel and heat treated to ensure adequate tensile strength. The tension bolt is secured using a lock-nut which is also made from the same material and heat treated identically. The ball bearing housing rests on a pedestal that is bolted to the test bed. The details of the bearing housing are shown in Figure 62 for clarity. An oil mist lubrication system is used to lubricate the ball bearings and the motor. The spent lubricant is extracted from the ball bearing housing through a port in the pedestal as shown in Figure 62.The bearing sleeve consisting of the foil bearing assembly is secured around the journal by a loading mechanism as shown in Figure 60. The loading mechanism consists of a frame structure which supports an I-beam on which 2 sets of pulleys are secured. The pulleys transmit load from a pneumatic actuator through a ¼" wire rope held taut by a turnbuckle as shown in Figure 61. The pneumatic actuator is controlled using a pressure regulator. The foil bearing assembly is loaded when the sleeve is moved in the vertical direction. Such a setup mimics the loading from a moving journal on a stationary sleeve. The HFS 4140 test journal is shown in Figure 63.

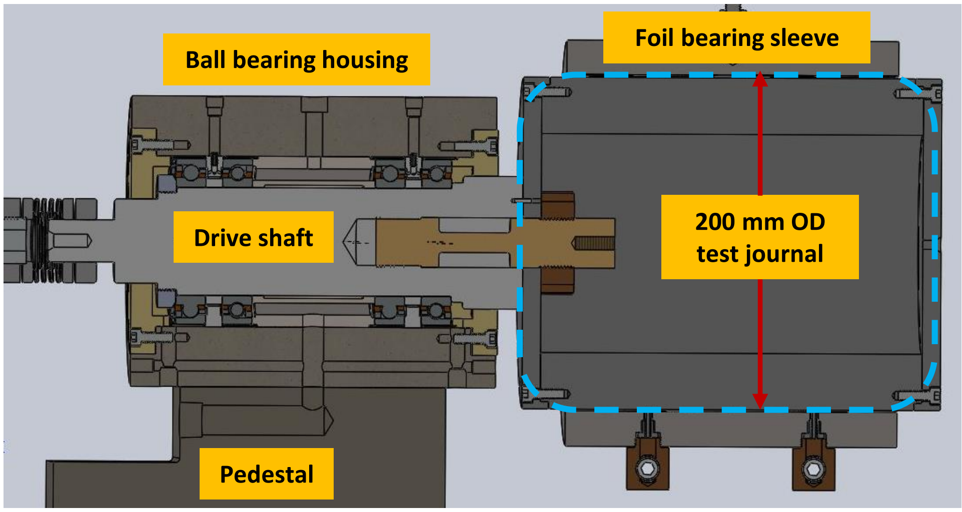

Figure 62 Sectional view of bearing housing

Figure 63 200 mm OD test journal

4.4 Instrumentation used for Data Acquisition

Schematic of the instrumentation for data acquisition is shown in Figure 64. Pressurized air (measured using an Omega^{TM} pressure transducer) is supplied to the foil bearing through the air pressure line in the laboratory. A torque rod connected to the sleeve transmits the friction torque to the load cell (Interface WMC 50). Another load cell (Interface WMC 2000) is employed to determine the loading on the bearing. Temperature measurement is carried out at 9 different locations on the sleeve using Type-K thermocouples. A flow meter (Hedland EZ) is used to determine the mass flow rate of air to the bearing. The offset and the gain for each instrument is determined from standard calibration methods and input into a LabView VI developed for recording and displaying test data. . The deflections of the journal and sleeve are found at 4 locations using proximity probes (Bentley Nevada) as shown in Figure 65. The probes numbered 1,3 and 4 are fixed to the ground while the probe 2 is fixed to the housing to measure relative displacement of the shaft when the sleeve is loaded.

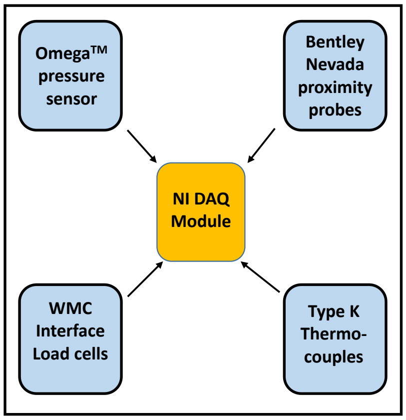

Figure 64 Schematic of the instrumentation used for data acquisition

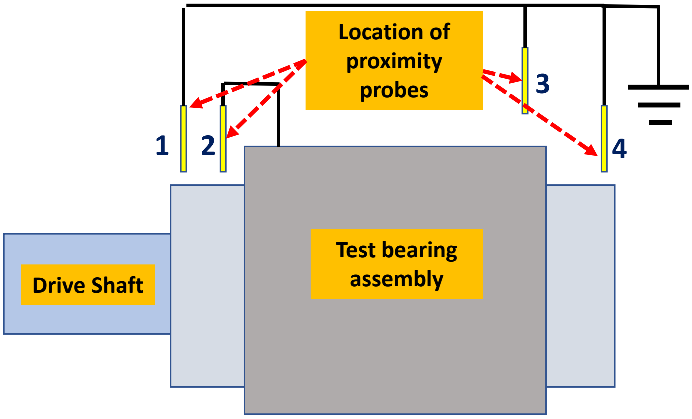

Figure 65 Location of proximity probes for measuring deflection

4.5 Results and Discussion of Experiments

Once the data acquisition system was checked and the instruments were inspected, three different sets of experiments were carried out. The first experiment determined the runout of the bearing. The bearing performance strongly depends on the operating clearance and run out directly affects the clearance of the bearing. For the second experiment, zero speed load deflection tests are conducted to characterize the stiffness of the bump structure. Finally, load capacity test was conducted for 2.76 bar supply pressure at very low rpm.

4.5.1 Shaft runout

Supply pressure of 1.38 bar was used to lift off the shaft and the unloaded shaft was slowly provided one complete rotation by hand. The displacements measured by proximity probes at location 1 and 4 provide insight into the run out of the shaft. The overall run out of the shaft was determined to be about 80 micron as shown in Figure 66.

.

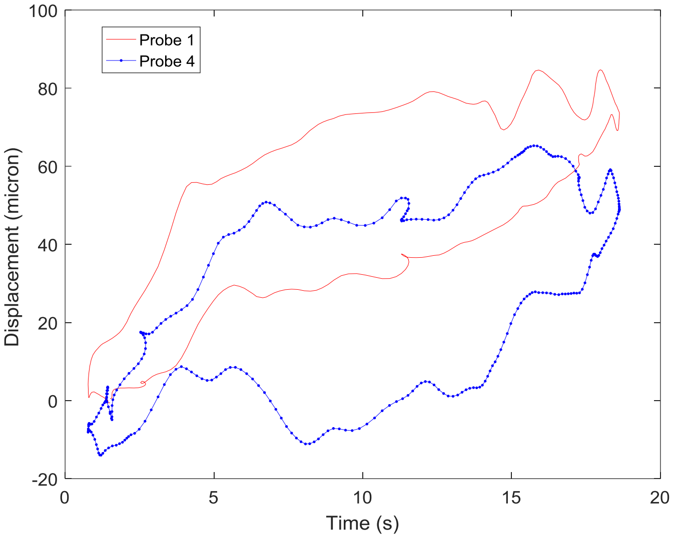

Figure 66 Run out of unloaded shaft with supply pressure of 1.38 bar

4.5.2 Load deflection test for stationary shaft

The zero speed load deflection test was carried out by applying load while keeping the bearing air supply valve closed. The bearing air supply valve was then opened and the tests were repeated under gauge pressures of 1.38 bar (20 psi) and 2.76 bar (40 psi) respectively.

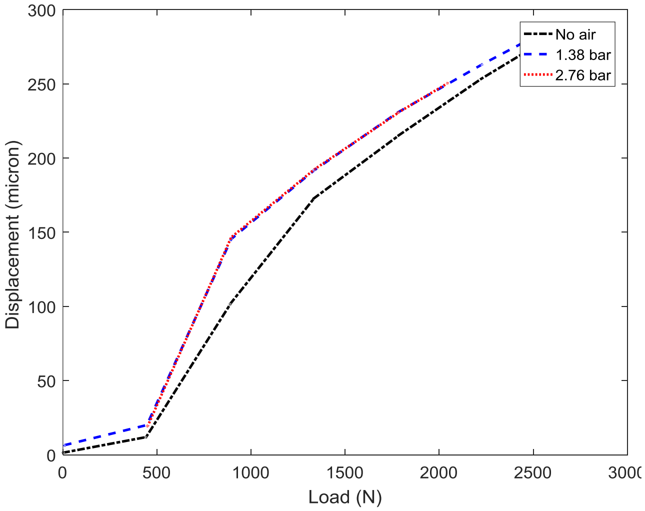

Figure 67 Shaft displacement measured using Probe 1 for non rotating shaft

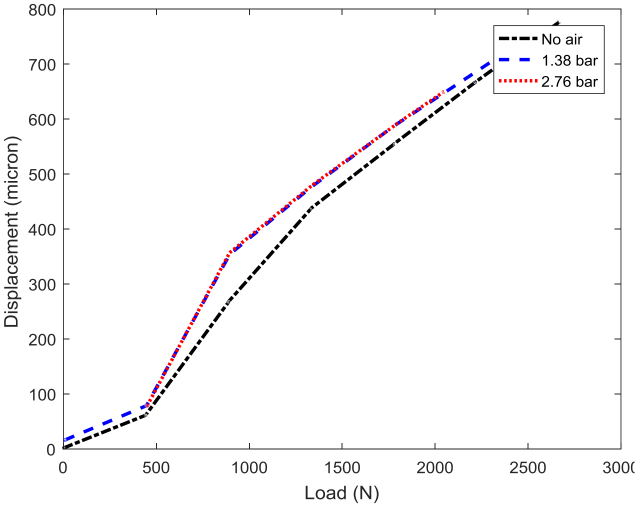

Figure 68 Shaft displacement measured using Probe 4 for non rotating shaft

It is noted that the same supply line was used to apply the load through the pneumatic actuator and also to supply pressurized air to the bearing. Consequently, the applied loading was limited by the pressure supplied to the bearing sleeve. Therefore, for a supply pressure of 2.76 bar, the maximum loading was limited to 2000 N. The displacements measured by probe 1 and probe 4 in Figure 67 and Figure 68 are absolute displacements at those locations and their profiles appear very similar. However, the magnitude of the displacement increases towards the free end of the shaft.

In Figure 69, the magnitude of displacement of the shaft relative to the bearing sleeve (measured by probe 2) is presented. Slope of the load versus displacement curve provides the bearing structural stiffness characteristics as shown in Figure 70. When no air is supplied to the bearing, the resulting load deflection curve yields the bump structural stiffness. When pressurized air is supplied to the bearing, the resulting load deflection curve yields the net stiffness coefficients of both hydrostatic air film and the underlying support structure.

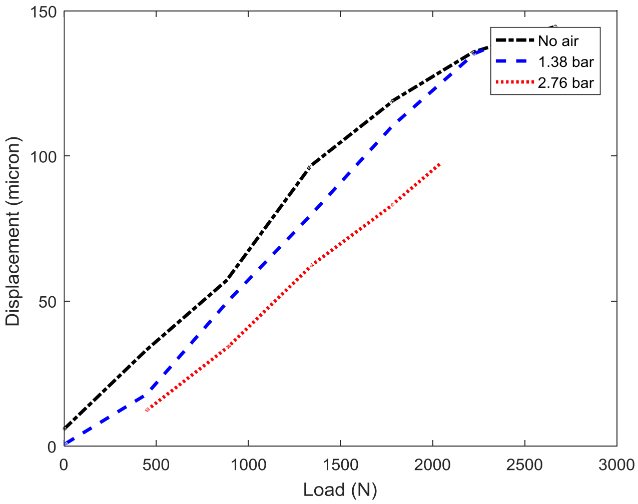

Figure 69 Load-deflection curves for HAFB with stationary shaft (Probe 2)

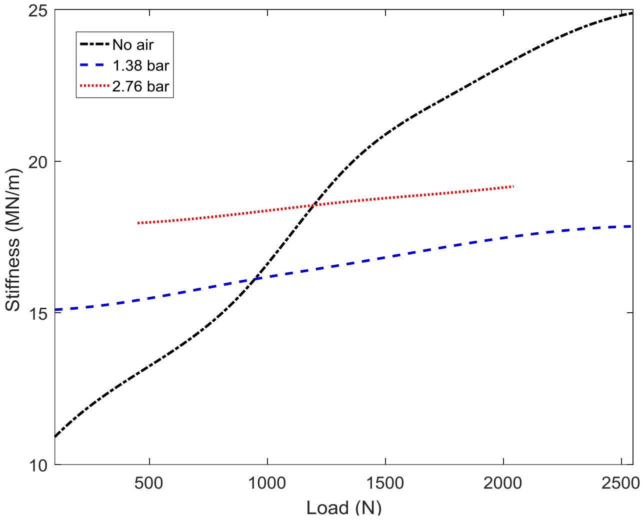

Figure 70 HAFB static stiffness with stationary shaft (from load deflection curves in Figure 69)

Under hydrostatic operation, the stiffness coefficients are larger than structural stiffness below about 1000 N for the case of 1.38 bar and about 1200 N for the case of 2.76 bar supply pressure. When air is injected into the orifices, the pressurized air facilitates better contact of the bumps with the sleeve and increases the effective contact area, thereby increasing the stiffness coefficients. Further, increase in supply pressure results in increased value of stiffness coefficients with applied load. The structural stiffness under no air for 2000 N is about 23.5 MN/m.

4.5.3 Load capacity for supply pressure of 2.76 bar

The shaft was slowly rotated by hand and the bearing was loaded while keeping the supply pressure at 2.76 bar. The displacements measured by proximity probes 1 and 4 are shown in Figure 71. The load capacity limit would be reached when the resistance to rotation (and temperature) drastically increases for a given load. However, before the load capacity could be reached, the maximum loading achievable with the pressure supply of 2.76 bar was reached (i.e. 2000 N). While this test does not provide the actual load capacity of the bearing, it does reaffirm the displacement trends observed in Figure 67 and Figure 68.

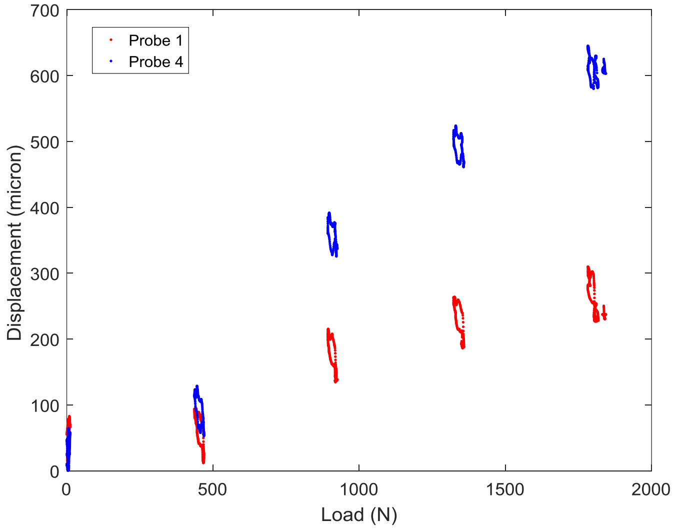

Figure 71 Shaft displacements under supply pressure of 2.76 bar

Chapter 5

CONCLUSIONS AND FUTURE WORK

Ref. [3] showed the usability of scaling laws for selecting radial clearance and support structure stiffness when an already existing, well designed, and well tested bearing is used as a reference. However, the practical application of the scaling laws for designing a bearing for a large system requires additional considerations including rotordynamic stability analysis.

A typical double overhang turbomachinery system supported by 2 radial foil bearings was used as a reference and the rotordynamic stability of scaled up systems employing the same configuration was determined. Simulations showed that the subsynchronous vibrations decrease as the bearing size increases. The strong stiffness anisotropy due to increased loading makes large foil bearings more stable than smaller bearings at comparable speeds of operation by increasing critical speeds.

In addition, the application of scaling laws was demonstrated for the first time by designing and testing 200 mm hybrid foil bearing system. Time domain simulations showed that a 200 mm hybrid bearing operating under 5 bar multipoint injection at 1000 rpm can support a load of 1961 N. Therefore, a 200 mm hybrid foil bearing and the corresponding test rig were designed and manufactured to verify the usability of the scaling laws. The maximum supply pressure in the experiment was 2.76 bar as the same supply line was used for loading the bearing.

Preliminary tests were conducted to characterize the bearing when subjected to loading with a stationary shaft. The structural stiffness with no air supplied is found to be 23.5 MN/m under 2000 N. The results obtained thus far demonstrate the challenges involved in working with large systems. Testing the foil bearing at high speed operation to expand the operating envelope of hybrid foil bearing systems is the scope of future work.

NOMENCLATURE

A_o = bearing surface area per support structure
C = nominal operating clearance
c_b = equivalent viscous damping coefficient
D = diameter of bearing
e = eccentricity
E = Young’s modulus
F = load capacity of bearing
f_b = pressure force on structure
g = acceleration due to gravity
$h(\theta, z_b)$ = local film thickness in the bearing
H = nondimensional film thickness
I_p = polar moment of inertia of the rotor
I_T = transverse moment of inertia of rotor
k_b = stiffness coefficient of support structure
$l_{ax,i}$ = axial location of imbalance from center of gravity
L = length of the bearing
$M_{\xi,\psi}$ = moments induced
m_r = rotor mass
N = shaft speed
O_{brg} = bearing center
P = nondimensional pressure
p_a = atmospheric pressure

p_{avg} = average bearing pressure

R = bearing radius

r_{cg} = centrifugal growth

r_p = preload

u_i = amount of imbalance

X, Y = rotor motion in radial direction

z = coordinate in axial direction

Z = nondimensional coordinate in axial direction

ξ, ψ = rotational coordinate

ξ_o = bearing load capacity coefficient

κ = ratio of specific heats

γ = offset ratio

δ = deflection of the structure

ε = nondimensional eccentricity

η = structural loss factor

θ = angular coordinate

ϕ_i = phase angle

Λ = bearing number

μ = dynamic viscosity of air

ν = Poisson’s ratio

ρ = density of shaft

τ = nondimensional time

ω = angular velocity of shaft

CONFLICT OF INTEREST STATEMENT

My advisor Dr. Daejong Kim has a potential research conflict of interest due to a financial interest with company Bellkim Energy LLC. A management plan has been created to preserve objectivity in research in accordance with UTA policy.

REFERENCES

[1] Bruckner, R., Jack, 2010, "An Assessment of Gas Foil Bearing Scalability and the Potential Benefits to Civilian Turbofan Engines," NASA/TM, 216732, Ohio.

[2] Agrawal, G., L., 1997, "Foil Air/Gas Bearing Technology ~ An Overview," International Gas Turbine & Aeroengine Congress & Exhibition, ASME, Orlando, Florida, 97-GT-347.

[3] Honavara Prasad, S., and Kim, D., 2016, "Scaling Laws for Radial Clearance and Support Structure Stiffness of Radial Foil Bearings," Journal of Engineering for Gas Turbines and Power.

[4] Raimondi, A. A., 1961, "A Numerical Solution for the Gas-Lubricated Full Journal Bearing of Finite Length," ASLE Transactions, 4pp. 131-155.

[5] DellaCorte, C., and Valco, M.J., 2000, "Load Capacity Estimation of Foil Air Journal Bearings for Oil-Free Turbomachinery Applications," NASA, NASA/TM-2000-209782, Ohio.

[6] DellaCorte, C., 2010, "Stiffness and Damping Coefficient Estimation of Compliant Surface Gas Bearings for Oil-Free Turbomachinery," NASA, NASA/TM-2010-216924, Ohio.

[7] Piekos, E. S., February 2000, "Numerical Simulation of Gas-Lubricated Journal Bearings for Microfabricated Machines," Department of Aeronautics and Astronautics, MIT.

[8] Peng, Z. C., and Khonsari, M. M., 2004, "Hydrodynamic Analysis of Compliant Foil Bearings with Compressible Air Flow," ASME Journal of Tribology, 126pp. 542-546.

[9] Peng, Z. C., and Khonsari, M. M., 2004, "On the Limiting Load-Carrying Capacity of Foil Bearings," ASME Journal of Tribology, 126pp. 817-818.

[10] Radil, K.C., Howard, S.A., and Dykas, B., 2002, "The Role of Radial Clearance on the Performance of Foil Air Bearings," NASA, NASA/TM-2002-211705, Ohio.

[11] Spakovszky, Z. S., and Liu, L. X., 2005, "Scaling Laws for Ultra-Short Hydrostatic Gas Journal Bearings," Journal of Vibration and Acoustics, 127(3) pp. 254-261.

[12] Rentzepis, G. M., and Sternlicht, B., 1962, "On the Stability of Rotors in Cylindrical Journal Bearings," ASME Journal of Basic Engineering, 84(4) pp. 521-531.

[13] Ausman, J. S., June 1961, "An Improved Analytical Solution for Self-Acting, Gas Lubricated Journal Bearings of Finite Length," Journal of Basic Engineering, 83(2)(Trans of the ASME, Series D) pp. 188-194.

[14] Ausman, J. S., 1963, "Linearized Ph Stability Theory for Translatory Half-Speed Whirl of Long, Self-Acting Gas-Lubricated Journal Bearings," ASME Journal of Basic Engineering, 85(4) pp. 611-618.

[15] Cheng, H. S., and Trumpler, P. R., 1963, "Stability of the High-Speed Journal Bearing Under Steady Load", Journal of Engineering for Industry, 85(3) pp. 274-279.

[16] Cheng, H. S., and Pan, C. H. T., March 1965, "Stability Analysis of Gas Lubricated, Self-Acting, Plain, Cylindrical, Journal Bearings of Finite Length, using Galerkin's Method," Journal of Basic Engineering, 87(1)(Trans of the ASME, Series D) pp. 185-192.

[17] Castelli, V., and Elrod, H. G., March 1965, "Solution of the Stability Problem for 360 Deg Self-Acting, Gas Lubricated Bearings," Journal of Basic Engineering, 87(1)(Trans of the ASME, Series D) pp. 199-212.

[18] Heshmat, H., and Xu, D., S., "Experimental investigation of 150 mm diameter large hybrid foil/magnetic bearing," Proceedings of the International Gas Turbine Congress 2003 Tokyo.

[19] Salehi, M., Heshmat, H., and Walton, J., F., 2007, "Advancements in the Structural Stiffness and Damping of a Large Compliant Foil Journal Bearing: An Experimental Study," ASME Journal of Engineering for Gas Turbines and Power, 129pp. 154-161.

[20] Ertas, B., Drexel, M., Van Dam, J., 2008, "A General Purpose Test Facility for Evaluating Gas Lubricated Journal Bearings," ASME Journal of Engineering for Gas Turbines and Power, 131(2) pp. 022502-022502-8.

[21] Delgado, A., 2015, "Experimental Identification of Dynamic Force Coefficients for a 110 mm Compliantly Damped Hybrid Gas Bearing," ASME Journal of Engineering for Gas Turbines and Power, 137(7) pp. 072502-072502-8.

[22] Kim, D., 2007, "Parametric Studies on Static and Dynamic Performance of Air Foil Bearings with Different Top Foil Geometries and Bump Stiffness Distributions," ASME Journal of Tribology, 129(2) pp. 354-364.

[23] Gunter, E. J., and Trumpler, P. R., 1969, "The Influence of Internal Friction on the Stability of High Speed Rotors with Anisotropic Supports," Journal of Engineering for Industry, 91(4) pp. 1105-1113.

[24] Childs, D., 1993, "Turbomachinery rotordynamics: phenomena, modeling, and analysis," Wiley, New York, .

[25] Timoshenko, S.P., and Goodier, J.N., 1970, "Theory of Elasticity," McGraw-Hill, New York, pp. 80-83.

[26] Honavara Prasad, S., and Kim, D., 2017, "Design approach for large foil bearings considering rotordynamics," ASME. Turbo Expo: Power for land, sea and air, 7A: Structures and Dynamics, pp. V07AT34A034.

[27] Kim, T., Ho, and Andres, L., San, 2009, "Effects of a Mechanical Preload on the Dynamic Force Response of Gas Foil Bearings: Measurements and Model Predictions," STLE Tribol. Trans., 52(4) pp. 569–580.

[28] Sim, K., Koo, B., Lee, J., Sung, 2014, "Effects of Mechanical Preloads on the Rotordynamic Performance of a Rotor Supported on Three-Pad Gas Foil Journal Bearings," ASME Journal of Engineering for Gas Turbines and Power, 136(12) pp. 122503-122503-8.

[29] Kim, D., Lee, A. S., and Choi, B. S., 2014, "Evaluation of Foil Bearing Performance and Nonlinear Rotordynamics of 120kW Oil-Free Gas Turbine Generator," Journal of Engineering for Gas Turbines and Power, 136(March).

[30] Kim, D., and Park, S., 2009, "Hydrostatic Air Foil Bearings: Analytical and Experimental Investigation," Tribology International, 42pp. 413-425.

[31] Kumar, M., August 2008, "Analytical and Experimental Investigations of Hybrid Air Foil Bearings,".

BIOGRAPHICAL INFORMATION

Srikanth Honavara Prasad is interested in various aspects of science and engineering. He received a Bachelor of Engineering degree in Mechanical Engineering from the Visvesvaraya Technological University in India. He completed his Master of Science degrees in both Mechanical and Aerospace Engineering at the University of Texas at Arlington.